The Astrophysical Journal, 902:82 (15pp), 2020 October 10 https://doi.org/10.3847/1538-4357/abb407

A Late-time Radio Survey of Short Gamma-ray Bursts at $z < 0.5$: New Constraints on the Remnants of Neutron-star Mergers

Genevieve Schroeder[1], Ben Margalit[2,8], Wen-fai Fong[1], Brian D. Metzger[3,4], Peter K. G. Williams[5,6], Kerry Paterson[1], Kate D. Alexander[1,8], Tanmoy Laskar[7], Armaan V. Goyal[1], and Edo Berger[5]
[1] Center for Interdisciplinary Exploration and Research in Astrophysics and Department of Physics and Astronomy, Northwestern University, 2145 Sheridan Road, Evanston, IL 60208-3112, USA
[2] Astronomy Department and Theoretical Astrophysics Center, University of California, Berkeley, Berkeley, CA 94720, USA
[3] Center for Computational Astrophysics, Flatiron Institute, 162 W. 5th Avenue, New York, NY 10011, USA
[4] Department of Physics and Columbia Astrophysics Laboratory, Columbia University, New York, NY 10027, USA
[5] Center for Astrophysics|Harvard & Smithsonian, 60 Garden Street, Cambridge, MA 02138, USA
[6] American Astronomical Society, 1667 K Street NW, Suite 800, Washington, DC 20006, USA
[7] Department of Physics, University of Bath, Claverton Down, Bath, BA2 7AY, UK
Received 2020 June 12; revised 2020 August 14; accepted 2020 August 30; published 2020 October 14

Abstract

Massive, rapidly spinning magnetar remnants produced as a result of binary neutron-star (BNS) mergers may deposit a fraction of their energy into the surrounding kilonova ejecta, powering a synchrotron radio signal from the interaction of the ejecta with the circumburst medium. Here, we present 6.0 GHz Very Large Array (VLA) observations of nine, low-redshift short gamma-ray bursts (GRBs; $z < 0.5$) on rest-frame timescales of ≈2.4–13.9 yr following the bursts. We place 3σ limits on radio continuum emission of $F_\nu \lesssim 6$–$20\ \mu$Jy at the burst positions, or $L_\nu \lesssim (0.6\text{–}8.3) \times 10^{28}$ erg s^{-1} Hz^{-1}. Comparing these limits with new light-curve modeling that properly incorporates relativistic effects, we obtain limits on the energy deposited into the ejecta of $E_{\rm ej} \lesssim (0.6\text{–}6.7) \times 10^{52}$ erg ($E_{\rm ej} \lesssim (1.8\text{–}17.6) \times 10^{52}$ erg) for an ejecta mass of $0.03\,M_\odot$ ($0.1\,M_\odot$). We present a uniform reanalysis of 27 short GRBs with 5.5–6.0 GHz observations, and find that $\gtrsim$50% of short GRBs did not form stable magnetar remnants in their mergers. Assuming short GRBs are produced by BNS mergers drawn from the Galactic BNS population plus an additional component of high-mass GW194025-like mergers in a fraction $f_{\rm GW190425}$ of cases, we place constraints on the maximum mass of a nonrotating neutron star (NS; Tolman–Oppenheimer–Volkoff mass; $M_{\rm TOV}$), finding $M_{\rm TOV} \lesssim 2.23\,M_\odot$ for $f_{\rm GW190425} = 0.4$; this limit increases for larger values of $f_{\rm GW190425}$. The detection (or lack thereof) of radio remnants in untargeted surveys such as the VLA Sky Survey (VLASS) could provide more stringent constraints on the fraction of mergers that produce stable remnants. If $\gtrsim$ 30–300 radio remnants are discovered in VLASS, this suggests that short GRBs are a biased population of BNS mergers in terms of the stability of the remnants they produce.

Unified Astronomy Thesaurus concepts: Gamma-ray bursts (629); Magnetars (992); Neutron stars (1108)

1. Introduction

The detection of gravitational waves (GWs) has enabled the first definitive discoveries of binary neutron-star (BNS) mergers (Abbott et al. 2017b, 2020). Of particular interest is the nature of the NS remnant produced by such mergers (e.g., Bernuzzi 2020) and how long it survives after the coalescence before collapsing to a black hole (BH), as this is directly tied to the luminosity and evolution of the resulting electromagnetic (EM) signature (e.g., Margalit & Metzger 2019). Among the many open questions is whether BH formation is always requisite for the production for an ultra-relativistic short gamma-ray burst (GRB) jet (e.g., Murguia-Berthier et al. 2017), or whether a long-lived magnetized NS remnant ("magnetar") could also be the engine of some bursts (e.g., Zhang & Mészáros 2001; Metzger et al. 2008; Mösta et al. 2020).

The nature of the merger remnant is particularly sensitive to the total initial mass of the binary, and indeed the first two BNS mergers, GW170817 and GW190425, had distinct total masses of $2.74^{+0.04}_{-0.01}\,M_\odot$ and $3.4^{+0.3}_{-0.1}\,M_\odot$, respectively (Abbott et al. 2017b, 2020), supporting the existence of diverse properties of the merger remnants and resulting EM signatures. The existence of an indefinitely stable, *hyper*- or *supra*massive NS remnant (where the difference depends on whether differential rotation is required to stabilize the remnant; e.g., Shibata & Taniguchi 2006) depends sensitively on the total mass of the system relative to various threshold masses that scale with the Tolman–Oppenheimer–Volkoff mass ($M_{\rm TOV}$; the maximum stable mass of a cold nonrotating NS). The most massive binaries are expected to undergo prompt collapse to a BH (e.g., Bauswein et al. 2013), while lower-mass binaries can remain stable for timescales significantly longer, until the critical amount of angular momentum is removed via magnetic-dipole spin-down. In some cases where the mass of the binary is sufficiently low, the merged object may remain indefinitely stable as an NS, even once it has spun down completely (e.g., Giacomazzo & Perna 2013).

The value of $M_{\rm TOV}$ is uncertain observationally but is of particular interest because it is sensitive to the unknown equation of state of the NS (Lattimer & Prakash 2016). Lower limits on $M_{\rm TOV}$ are available from the masses of pulsars, with the most constraining at present being $M_{\rm TOV} > 2.14^{+0.09}_{-0.10} M_\odot$ from the mass of J0740 + 6620 (Cromartie et al. 2020). However, BNS mergers offer one of the few potential probes of *upper* limits on $M_{\rm TOV}$ (e.g., Lawrence et al. 2015; Margalit & Metzger 2017; Shibata et al. 2019).

[8] NASA Einstein Fellow.

If the merger remnant survives even for a brief period of time, the additional reservoir of rotational energy—if coupled effectively to its surroundings—will substantially boost the kinetic energy of the merger ejecta. As the latter interacts with the circum-merger environment, it will decelerate via a shock, generating synchrotron emission that is predicted to peak at approximately gigahertz frequencies on approximately year timescales, depending on the properties of the shock and the environment (Nakar & Piran 2011). As pointed out by Metzger & Bower (2014), this signal could be greatly enhanced in the case of a long-lived magnetar remnant relative to mergers that result in prompt BH formation. The existence of a long-lived NS remnant can also have a significant effect on the color and evolution of the resulting "kilonova" signature (Yu et al. 2013; Metzger & Fernández 2014; Kasen et al. 2015), as well as the early-time X-ray signatures of the merger (e.g., Metzger & Piro 2014), which can in principle be probed by follow-up observations of GW events.

Cosmological, short-duration GRBs, which are detected to $z \approx 2$ (Fong et al. 2017) and originate from BNS (and/or possibly NS–BH) mergers (Berger 2014; Abbott et al. 2017a; Gompertz et al. 2020), provide a promising route to place constraints on the nature of the remnant. They have been discovered and well-localized since 2004 by NASA's Neil Gehrels Swift Observatory (Gehrels et al. 2004) and provide the necessary long time baseline required to match the ≈1–10 yr peak timescales of the predicted radio signatures. Indeed, previous radio studies of short GRBs on year to several-year timescales after the events have endeavored to constrain the nature of the BNS remnant. All such studies have yielded non-detections, translating to upper limits on the kinetic energy scales of $\lesssim 10^{53}$–10^{54} erg (Metzger & Bower 2014; Fong et al. 2016b; Horesh et al. 2016; Klose et al. 2019; Liu et al. 2020). A few of these studies were based on simpler analytical models (Nakar & Piran 2011) that break down in the low-density, low ejecta mass regime in which relativistic effects are increasingly important. Recent modeling developments that have incorporated relativistic effects and the "deep-Newtonian" regime, coupled with deeper observations, have placed constraints on the energy imparted from the remnant of $\lesssim 10^{52}$ erg. Some previous studies have concentrated on those with anomalous X-ray emission, X-ray "plateaus," or extended emission (Metzger & Bower 2014; Fong et al. 2016b), as these have been attributed to the formation of magnetars (Bucciantini et al. 2012). Others have focused on short GRBs with candidate kilonovae (Horesh et al. 2016) or radio continuum surveys of short GRBs to look for optically obscured star formation (Klose et al. 2019).

Here, we take a different approach from previous studies, and target low-redshift short GRBs ($z \lesssim 0.5$), agnostic to their X-ray behavior or association to kilonovae. Assuming that these events are associated with BNS mergers, they provide the deepest constraints on the fate of the remnant that can be attained from the short GRB population. In Section 2, we present the details of our observations of nine short GRBs and introduce additional literature data at 1–6 GHz. In Section 3, we introduce our new light-curve model for highly energetic kilonova ejecta. In Section 4, we use our radio limits and the literature data, along with our new light-curve modeling, to determine the allowed ejecta kinetic energies $E_{\rm ej}$ from short GRBs. In Section 5, we compare the maximum kinetic energies $E_{\rm ej,max}$ to theoretical expectations to place constraints on $M_{\rm TOV}$, and explore the role of high-mass, GW190425-like mergers. In Section 6, we explore future observational prospects in constraining BNS remnants, with a focus on observations of cosmological short GRBs, follow-up of GW events, and searches in untargeted radio surveys. We end with a summary and our conclusions in Section 7. In this paper, we employ a standard cosmology of $H_0 = 69.6$ km s^{-1} Mpc^{-1}, $\Omega_M = 0.286$, and $\Omega_{\rm vac} = 0.714$ (Bennett et al. 2014).

2. Observations

2.1. Sample

Our sample comprises nine low-redshift short GRBs discovered by the Swift/Burst Alert Telescope (BAT; Gehrels et al. 2004). The redshifts, determined from the spectroscopic redshifts of their host galaxies, are $z \approx 0.16$–0.46 (Table 1; Gehrels et al. 2005; Bloom et al. 2006, 2007; Perley et al. 2012; Cucchiara et al. 2013; Wiersema et al. 2013; de Ugarte Postigo et al. 2014; Chornock & Fong 2015; Castro-Tirado et al. 2015; Troja et al. 2016; Lamb et al. 2019). This sample represents most of the known Swift short GRBs discovered in 2005–2016 with $z \lesssim 0.45$ and sky locations observable with the Very Large Array (VLA). Based on their BAT gamma-ray light curves, the durations of eight of the bursts are $T_{90} = 0.024$–1.20 s (15–350 keV) while GRB 150424A is classified as a short GRB with extended emission (Norris et al. 2015; Lien et al. 2016), resulting in a measured $T_{90} = 81.0$ s. Comparing their gamma-ray properties to the Swift GRB population, all of these events are classified as short-duration, spectrally hard GRBs.

Four of the events in the sample have subarcsecond localization from the detection of optical afterglows (GRBs 130603B, 140903A, 150424A, and 160821B) while the remaining five events have positional uncertainties of $\sim 2''$ from the detection of their X-ray afterglows (Evans et al. 2009). Two events, GRBs 130603B and 160821B, have detected kilonova counterparts based on their multiband photometry, with inferred ejecta masses of 0.03–0.08 $M_\odot$ and 0.011 $M_\odot$, respectively (Berger et al. 2013; Tanvir et al. 2013; Lamb et al. 2019).

2.2. VLA Observations

We observed the positions of nine short GRBs with the Karl G. Jansky VLA. Observations took place between 2019 January 4 and February 5 UT in either the C-configuration or the hybrid CnB configuration (PI: Fong, Program 18B-168). Each target was observed for two hours at a mean frequency of 6.0 GHz (with lower side-bands and upper side-bands centered at 4.9 GHz and 7.0 GHz, respectively). We used the Common Astronomy Software Application (CASA) pipeline products for data calibration and analysis (McMullin et al. 2007), using 3C147, 3C286, and 3C48[9] for flux calibration, and standard sources in the VLA calibrator catalog for gain calibration. We used CASA/`tclean` to image the sources, employing Briggs weighting with a robust parameter of 0.5. The average beam size of the observations is $4\farcs6 \times 2\farcs9$. The details of the observations are listed in Table 1. Other than for GRB 100206A (described below), we do not detect any radio sources in or around the GRB positions.

[9] Since 2018 January, 3C48 has undergone flaring, which may affect the flux calibration at a level of $\lesssim$5%. We use 3C48 only for one event, GRB 060502B, and expect the effect to be negligible.

Table 1
Log of 6.0 GHz VLA Observations of Short GRBs

GRB	z	UT date	$\delta t_{\rm rest}$ (yr)	F_ν (μJy)	L_ν (erg s^{-1} Hz^{-1})
GRB 050509B	0.225	2019 Jan 10.592	13.683	<7.8	$<1.2 \times 10^{28}$
GRB 060502B	0.287	2019 Jan 11.942	12.705	<6.6	$<1.7 \times 10^{28}$
GRB 100206A	0.41	2019 Jan 4.988	8.598	<8.1	$<4.9 \times 10^{28}$
GRB 130603B	0.356	2019 Jan 12.587	5.614	<12.3	$<5.4 \times 10^{28}$
GRB 130822A	0.154	2019 Jan 6.941	5.379	<8.7	$<5.7 \times 10^{27}$
GRB 140903A	0.351	2019 Feb 5.391	4.427	<19.5	$<8.3 \times 10^{28}$
GRB 150120A	0.46	2019 Jan 14.063	3.986	<6.3	$<5.1 \times 10^{28}$
GRB 150424A	0.3[a]	2019 Feb 5.308	3.789	<9.0	$<2.6 \times 10^{28}$
GRB 160821B	0.16	2019 Jan 8.021	2.382	<8.1	$<5.8 \times 10^{27}$

Notes. Upper limits correspond to 3σ confidence.
[a] The redshift of $z = 0.3$ quoted for GRB 150424A is based on an association with a bright, nearby galaxy (Castro-Tirado et al. 2015). However it is possible that the burst is instead associated with a fainter galaxy at $z \approx 1$ (Knust et al. 2017; Jin et al. 2018). For this paper, we assume $z = 0.3$.
References for redshifts. (1) Bloom et al. (2006), (2) Gehrels et al. (2005), (3) Bloom et al. (2007), (4) Perley et al. (2012), (5) Cucchiara et al. (2013), (6) de Ugarte Postigo et al. (2014), (7) Wiersema et al. (2013), (8) Troja et al. (2016), (9) Chornock & Fong (2015), (10) Castro-Tirado et al. (2015), (11) Lamb et al. (2019).

At the position of GRB 140903A, there is severe contamination by the side-lobes of an unrelated 11.3 mJy source, NVSS 155207 + 273501 (Condon et al. 1998), within the pointing field of view. To mitigate the effects of the bright source, the field of GRB 140903A was calibrated and imaged outside of the standard NRAO pipeline in order to apply a peeling algorithm (Noordam 2004; Intema et al. 2009) to reduce the side-lobes of the source. The data were reduced in the CASA framework using standard calibrations and automatic radio frequency interference flagging with the `aoflagger` program (Offringa et al. 2010, 2012). After an initial round of calibration, the bright source was subtracted using the "rubbl-rxpackage peel" workflow described in Williams et al. (2019). The peeled visibilities were then inverted using multifrequency synthesis (Sault & Wieringa 1994) to create an image of 1201 pix^2, each pixel $0\farcs5$ on a side. After removing the contaminating effects of this source, we did not detect a radio source at the position of GRB 140903A.

To obtain the rms ($\sigma_{\rm rms}$) of each image, we used the `imtool` package within `pwkit` on source-free regions around the position of each GRB (Williams et al. 2017). We found $\sigma_{\rm rms} = 2.1$–$6.5\ \mu$Jy, resulting in 3σ upper limits on the flux density of $F_\nu \lesssim 6.3$–$19.5\ \mu$Jy.

For GRB 100206A, we detected a source at R.A. $= 3^{\rm h}08^{\rm m}39\fs163$, decl. $= +13°09'29\farcs18$ on the outskirts of the XRT position (90% confidence; Evans et al. 2009). This position is coincident with the centroid of the host galaxy, which is classified as a luminous infrared galaxy (Perley et al. 2012). Employing a point-source model with `imtool`, we measured $F_\nu = 60.4 \pm 5.0\ \mu$Jy. We note that the radio flux measured is consistent with observations taken 5 yr prior (Klose et al. 2019), and we attribute this emission to star formation in the host galaxy. Using standard relations between the radio flux and star formation rate (SFR; Yun & Carilli 2002; Perley & Perley 2013), we derive SFR $= 78 \pm 6.5\ M_\odot$ yr^{-1}, roughly twice the SFR derived from the optical spectroscopy of 20–40 $M_\odot$ yr^{-1} (Perley et al. 2012), indicative of obscured star formation. This result is also 1.3 times higher than the determination from radio observations of $59 \pm 10\ M_\odot$ yr^{-1} (Klose et al. 2019), with the discrepancy due to minor differences in SFR relations used. No other radio sources are found in or near the XRT position, and we thus derive a 3σ limit of $F_\nu \lesssim 8.1\ \mu$Jy for GRB 100206A.

Using the redshift of each burst, we calculate the spectral luminosity, L_ν, as well as the rest-frame time of the observation since the Swift/BAT trigger, $\delta t_{\rm rest}$. The observations, along with model light curves (Section 4.1) are shown in Figure 1.

2.3. Literature Data

To supplement our low-redshift sample, we collect all available radio limits following short GRBs on $\delta t_{\rm rest} \gtrsim 0.1$ yr timescales from the literature. We include nine limits at 1.4, 2.1, and 3.0 GHz (Metzger & Bower 2014; Horesh et al. 2016), 17 limits at 5.5 GHz (Klose et al. 2019), and nine limits at 6.0 GHz from our previous work (Fong et al. 2016b). For each burst, we compute the 3σ limit in flux density, and use the redshift of the burst to convert to a 3σ upper limit in L_ν. When considering both this work and the literature sample, there are multiple observations for seven events (GRBs 050724, 070724A, 051221A, 060502B, 100206A, 130603B, and 150424A). The total number of short GRBs with deep observations on these timescales is thus 27 bursts. The literature data are also shown in Figure 1.

3. Light-curve Modeling

In the following, we discuss our new light-curve modeling. Compared to the analytic framework first laid out by Nakar & Piran (2011), our present models incorporate the full dynamics of a single-velocity-shell ejecta including the transition between coasting and decelerating phases, relativistic dynamics, relativistic timing and Doppler effects on the light curve, and the deep-Newtonian regime. These factors combined have important effects on the pre-peak behavior of the light curves. A similar model was also recently applied by Liu et al. (2020) to a sample of previously published short GRB radio limits, and we provide a comparison in Section 6.

The radio signatures of kilonovae ejecta were first discussed by Nakar & Piran (2011) who showed that this emission typically peaks at the deceleration time, $t_{\rm dec}$, at which the ejecta dynamics transition from the coasting ejecta-dominated phase to the Sedov–Taylor phase. Nakar & Piran (2011) discussed the case of nonrelativistic ejecta ($\Gamma\ \beta \lesssim 1$) relevant to the initial ejection velocities of material from BNS mergers. The deposition of additional energy into this ejecta by a long-lived

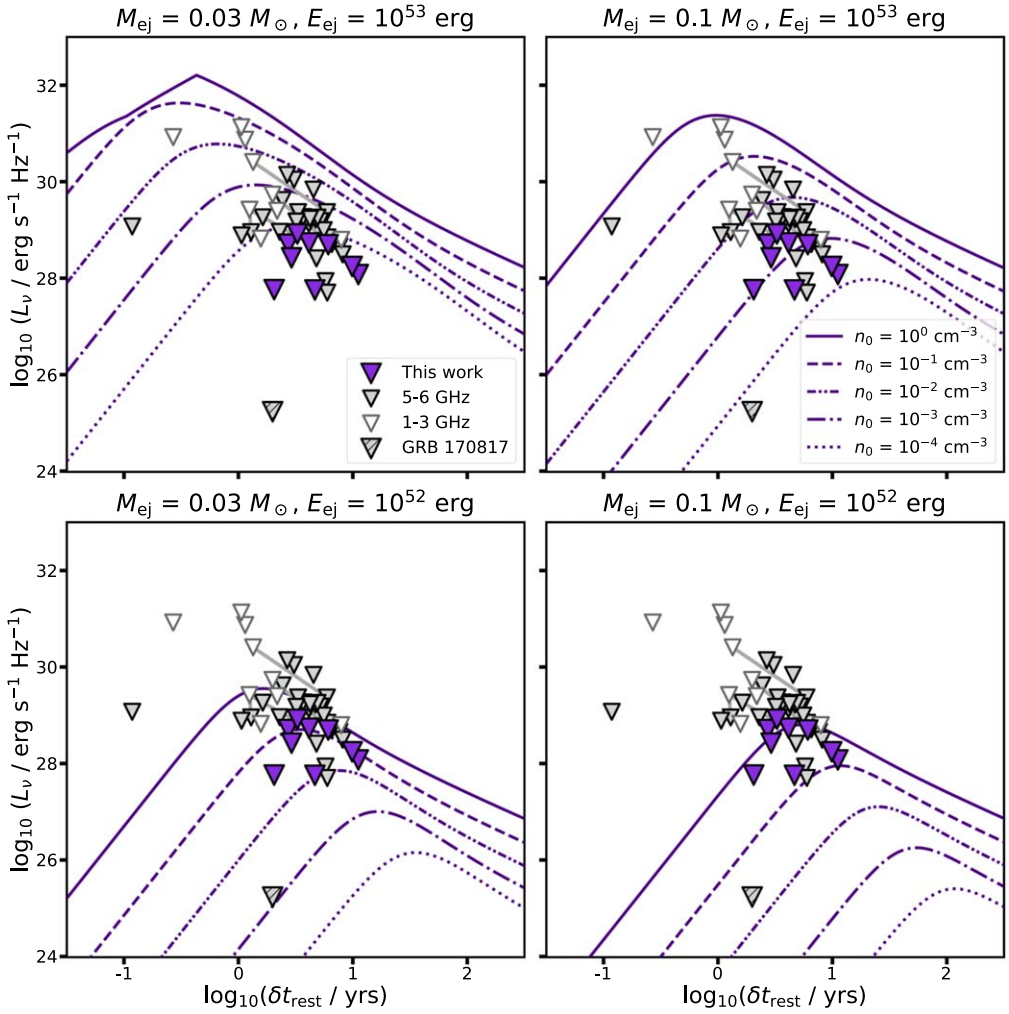

Figure 1. 6.0 GHz spectral luminosity, L_ν vs. rest-frame time $\delta t_{\rm rest}$ of the nine low-z short GRBs in our sample (purple triangles), where triangles denote 3σ upper limits. Also shown are all short GRBs with radio observations at $\delta t_{\rm rest} \gtrsim 0.1$ yr taken at 5.5 GHz and 6.0 GHz with ATCA and the VLA (gray triangles; Fong et al. 2016b; Klose et al. 2019) and with the VLA at 1–3 GHz (open gray triangles; Metzger & Bower 2014; Horesh et al. 2016). Lines connect observations for the same burst. These limits are compared to 6.0 GHz light-curve models computed for two sets of fixed ejecta mass $M_{\rm ej} = 0.03$ and $0.1\,M_\odot$ and ejecta energies $E_{\rm ej} = 10^{52}$ and 10^{53} erg at varying densities of $n_0 = 10^{-4} - 1$ cm^{-3}, and fixed parameters $p = 2.4$, $\epsilon_e = 0.1$, $\epsilon_B = 10^{-2}$. We note that a direct comparison to the 1–3 GHz limits requires an increase to the models by a small correction factor of $\lesssim 3$ ($\propto \nu^{-(p-1)/2}$). However, we show all existing radio limits here for completeness. Also shown is the latest published 6.0 GHz limit for GW170817 (hatched triangle; Hajela et al. 2019).

magnetar remnant would accelerate this ejecta to potentially relativistic velocities. As this is precisely the scenario we wish to constrain, we extend the Nakar & Piran (2011) model to account for relativistic dynamics of the ejecta and relativistic effects on the resulting light curve (see also Hotokezaka & Piran 2015; Horesh et al. 2016; Liu et al. 2020).

The dynamics of an ejectum with kinetic energy $E_{\rm ej}$ and mass $M_{\rm ej}$ depend on its initial Lorentz factor $\Gamma_0 = 1 + E_{\rm ej}/M_{\rm ej}c^2$ and corresponding velocity $\beta_0 c = c(1 - \Gamma_0^{-2})^{1/2}$, in combination with the ambient density n_0. With these parameters, the characteristic timescale (in the observer frame) at which the radio light curve peaks is (Hotokezaka & Piran 2015)

$$t_{\rm dec} \sim \left(\frac{3E_{\rm ej}}{4\pi m_p c^5 n_0 \Gamma_0(\Gamma_0 - 1)\beta_0^3}\right)^{1/3} \frac{(1+z)}{\Gamma_0^2}, \quad (1)$$

where the final term $(1+z)/\Gamma_0^2$ is responsible for transforming between the blast-wave rest frame and the observer frame, and accounts for cosmological redshift of the source.

We model the ejecta dynamics within the "homogeneous shell approximation" following Pe'er (2012; see also Huang et al. 1999; Nava et al. 2013). This one-zone model allows us to numerically integrate the forward-shock dynamics for arbitrary Γ_0 and correctly reproduce the coasting phase at $t \ll t_{\rm dec}$ and Blandford–McKee (Sedov–Taylor) solutions in the ultra-relativistic (nonrelativistic) regimes at $t \gg t_{\rm dec}$.

We calculate synchrotron emission from the shocked material assuming electrons at the shock-front are accelerated into a nonthermal population that shares a fraction ϵ_e of the shock power, and that magnetic fields are amplified behind the shock-front such that $B = \sqrt{8\pi\epsilon_B u_{\rm th}}$ where $u_{\rm th}$ is the post-shock thermal energy density and ϵ_B a constant <1 (e.g., Sari et al. 1998).

We account for effects of the deep-Newtonian regime on the nonthermal electron distribution (Sironi & Giannios 2013), relevant when the ejecta velocity is $\lesssim 0.2c(\bar{\epsilon}_e/0.1)^{-1/2}$, where $\bar{\epsilon}_e \equiv 4\epsilon_e(p-2)/(p-1)$ and $2 < p < 3$ is the power-law index describing the nonthermal electron distribution,

$dN_e/d\gamma \propto \gamma^{-p}$ at $\gamma \geqslant \gamma_m$ (where γ is the electron Lorentz factor). In what follows we assume a value of $\epsilon_e = 0.1$, motivated by the findings of first-principles particle-in-cell numerical simulations into weakly magnetized plasma characteristic of the inter-stellar medium (e.g., Spitkovsky 2008). In the deep-Newtonian regime, the minimal Lorentz factor of shock-accelerated electrons is $(\gamma_m - 1) \lesssim 1$, and only a small fraction of electrons are accelerated to $\gamma \gtrsim 2$, where they can emit synchrotron radiation. This has an important impact on the resulting radio light curves.

For most of the physically relevant parameter space, emission at approximately gigahertz radio frequencies is in the slow-cooling optically thin regime; however our model also fully allows for fast-cooling electrons (following Sari et al. 1998). Synchrotron self-absorption is taken into account in an approximate manner,[10] by limiting the spectral luminosity to a maximum defined by $L_\nu = 8\pi^2\Gamma R^2 kT(\gamma)\nu'^2/c^2$ where R is the blast-wave radius, $kT(\gamma) \approx \gamma m_e c^2/3$, $\gamma = \max[\gamma_m, (2\pi m_e c\nu'/eB)^{1/2}]$, and ν' is the emission frequency in the blast-wave rest frame, related to the observed frequency through $\nu' \approx \nu\Gamma(1-\beta)(1+z)$. We find that synchrotron self-absorption is only relevant in a small subset of cases where the initial ejecta Lorentz factor is very large (large $E_{\rm ej}$ and small $M_{\rm ej}$).

Compared to the Nakar & Piran (2011) analytic models that were used in Metzger & Bower (2014), Fong et al. (2016b), and Klose et al. (2019), relativistic effects (for high $E_{\rm ej}$) cause the light curve to peak earlier (by a factor of $\sim\Gamma_0^{-8/3}$; Equation (1)) and at a larger flux. Relativistic effects were first accounted for by Horesh et al. (2016), with a slightly different dynamical model than we adopt here. Their model, based on Piran et al. (2013), produces the correct temporal scaling laws in the coasting, Blandford–McKee, and Sedov–Taylor regimes, however may differ by factors of the order of unity from the exact quantitative dynamics implied by these analytic solutions. The strong dependence of the radio luminosity on blast-wave velocity ($\propto\beta^{(5p-3)/2}$ in the nonrelativistic non-deep-Newtonian regime) implies that even a factor of ∼two difference in velocity can amount to an ≳order-of-magnitude difference in luminosity. We have carefully verified that our model asymptotes to the exact coasting/Blandford–McKee/Sedov–Taylor solutions in the appropriate limits, including subtleties of distinguishing between ejecta (contact discontinuity) and shock velocities that are neglected in some models.

As in previous work, our model assumes spherical symmetry (though see Margalit & Piran 2015) and does not account for velocity-structure of the ejecta. The latter amounts to a conservative assumption: a radial velocity profile would enhance the early ($\lesssim t_{\rm dec}$) light curve, leading to more stringent upper limits on $E_{\rm ej}$.

Finally, we note that our model is geared toward constraining highly energetic kilonova ejecta due to possible magnetar energy deposition. Radio emission from "normal" kilonovae ejecta, with $E_{\rm ej} \sim 10^{51}$ erg, may in fact be inhibited for a significant period of time due to interaction of the GRB jet with the ambient medium ahead of the ejecta (Margalit & Piran 2020). Our model does not account for this effect, which is likely negligible for highly energetic (fast) ejecta.

[10] This approximation is correct to within an order-unity factor (dependent on p) of the full treatment of synchrotron self-absorption in the nonrelativistic spherical regime and suffices for the purposes of our present work (and see Granot et al. 1999 for a relativistic treatment).

4. Short GRB Remnant Kinetic Energy Constraints

Here, we use the radio limits derived in Section 2 and the light-curve modeling described in Section 3 to constrain the magnetar remnant energy that is transferred to the ejecta as kinetic energy ($E_{\rm ej}$) in short GRBs.

4.1. Light-curve Comparisons

We generate model light curves for a range of circumburst densities to represent those inferred from broadband analysis of short GRB afterglows, $n_0 = 10^{-4}$–1 cm^{-3} (Figure 1; Fong et al. 2015). We compute light curves for two sets of ejecta masses, $M_{\rm ej} = 0.03\,M_\odot$ and $0.1\,M_\odot$, which are chosen to represent the range of inferred ejecta masses for kilonovae following short GRBs (Ascenzi et al. 2019) and GW170817 ($M_{\rm ej} \approx 0.05\,M_\odot$; Villar et al. 2017; Arcavi 2018). We also choose two fiducial kinetic energies deposited into the ejecta, $E_{\rm ej} = 10^{52}$ and 10^{53} erg, where the former represents a typical energy extractable from a supramassive NS (e.g., Margalit & Metzger 2019), while the latter represents the maximum energy that can be extracted from a magnetar with $M = M_{\rm TOV} \sim 2.2\,M_\odot$ (Metzger et al. 2015a). We fix the values of $\nu = 6$ GHz, $p = 2.4$, $\epsilon_e = 0.1$, $\epsilon_B = 10^{-2}$, and $\zeta_e = 1$, where ζ_e is the fraction of electrons participating in diffusive shock acceleration out of total electrons. The resulting model light curves (L_ν versus $\delta t_{\rm rest}$), grouped by ejecta mass and ejecta energies, are displayed in Figure 1.

As expected, we find that the radio signal is brightest for the $M_{\rm ej} = 0.03\,M_\odot$ and $E_{\rm ej} = 10^{53}$ erg case, and the predicted luminosities decrease for larger values of ejecta mass and lower ejecta energies. In addition, for a given set of fixed parameters, the peak timescales increase as density decreases; this can be intuitively explained since shocks in lower-density environments take longer to sweep up a mass comparable to their own (Equation (1)). A basic comparison to the low-redshift short GRB limits shows that in the most optimistic case, models with extremely low densities of $n_0 \gtrsim 10^{-4}$ cm^{-3} are ruled out. Moreover, in the most pessimistic case ($M_{\rm ej} = 0.1\,M_\odot$, $E_{\rm ej} = 10^{52}$ erg), the low-redshift short GRB limits still provide meaningful constraints of $n_0 \lesssim 0.1$–1 cm^{-3} (Figure 1). Overall, the short GRB limits presented here, in the context of new light-curve modeling, are significantly more constraining than many previous works (Metzger & Bower 2014; Fong et al. 2016b; Klose et al. 2019; Liu et al. 2020).

4.2. Afterglow Parameter Constraints

Since there are degeneracies between model parameters, we first collect available constraints on the values of p, ϵ_B, and n_0 from existing broadband afterglow fitting. For the low-redshift sample presented here, only two GRBs have previously determined values, GRB 130603B and GRB 140903A. For GRB 130603B, $n_0 = 0.31^{+0.08}_{-0.04}$ cm^{-3} and $p = 2.70$ ($\epsilon_e = 0.1$, $\epsilon_B = 10^{-2}$), and for GRB 140903A, $n_0 = 3.40^{+2.9}_{-1.6} \times 10^{-3}$ cm^{-3} and $p = 2.27$ ($\epsilon_e = 0.1$, $\epsilon_B = 10^{-3}$; Fong et al. 2015).

For GRBs 050509B, 150424A, and 160821B, we use available afterglow data at early times to place constraints on these parameters. We use the standard synchrotron model for a relativistic blast-wave (Granot & Sari 2002), which provides a mapping of the afterglow spectral and temporal evolution to the isotropic-equivalent afterglow kinetic energy ($E_{\rm K,iso}$), n_0, ϵ_e, and ϵ_B. In general, we choose fiducial values for the microphysical parameters. In particular, we fix $\epsilon_e = 0.1$,

motivated both observationally with GRB afterglow fitting, which finds $\epsilon_e \sim 0.1$ (Panaitescu & Kumar 2001; Ryan et al. 2015; Beniamini & van der Horst 2017), and theoretically by first-principles particle-in-cell simulations, which find ~10% of the kinetic energy from shocks can be deposited into nonthermal particles (Spitkovsky 2008). For ϵ_B, short GRBs with broadband afterglow detections (radio, optical, and X-rays) tend to favor values $\epsilon_B < 0.1$ for fixed $\epsilon_e = 0.1$; although models with $\epsilon_B < 10^{-3}$ are routinely found to provide inadequate matches to the broadband data (Fong et al. 2015). Thus, we employ a fiducial value of $\epsilon_B = 10^{-2}$ unless otherwise stated. Finally, we choose a fiducial value of $p = 2.4$, motivated by the median value found for short GRBs (Fong et al. 2015).

For GRB 050509B, we use the X-ray afterglow detection (Swift/XRT; Gehrels et al. 2005), as well as the optical (Bloom et al. 2006) and radio upper limits (van der Horst et al. 2005) to determine a value of $p = 2.52$ and a limit on the circumburst density of $n_0 \lesssim 0.55$ cm^{-3} for $\epsilon_e = 0.1$, $\epsilon_B = 10^{-2}$ (Table 2). For GRB 150424A, we use the X-ray (Evans et al. 2009), optical (Marshall & Beardmore 2015), and 9.8 GHz VLA (Program 15A-235; updated from Fong 2015) afterglow detections to determine a value of $p = 2.40$ and a low density of $n_0 = 1.98^{+4.4}_{-1.4} \times 10^{-4}$ cm^{-3} (assuming $\epsilon_e = 0.1$, $\epsilon_B = 10^{-2}$). Finally, for GRB 160821B, we use the X-ray (Evans et al. 2009), optical (Lamb et al. 2019), and 5.0 GHz VLA detection (Program 15A-235; updated from Fong et al. 2016a) to determine $p = 2.36$ and $n_0 = 0.13^{+0.05}_{-0.04}$ cm^{-3} (assuming $\epsilon_e = 0.1$, $\epsilon_B = 10^{-2}$; Table 2).

For the remaining short GRBs in the low-redshift sample, the afterglow data are too sparse to adequately constrain these parameters. Thus, we assume fiducial values for these bursts (Table 2 and Section 4.3). We also collect measurements or constraints on the values of p and n_0 for 18 additional short GRBs with radio limits at 5.5 and 6.0 GHz (Fong et al. 2016b; Klose et al. 2019) from Fong et al. (2015). The afterglow parameters for all short GRBs used in this work are summarized in Table 2.

4.3. Inferred Limits on Ejecta Kinetic Energies

We next compare the late-time radio observations to a combination of the deposited energy $E_{\rm ej}$ and circumburst density n_0, by determining the parameter space ruled out by each 6.0 GHz limit. For each short GRB in the low-redshift sample, we generate a grid of 62,500 models with the appropriate values of p and ϵ_B inferred from the broadband afterglow, with $\epsilon_e = 0.1$ and $\zeta_e = 1$ (Table 2). For bursts that lack available information, we assume fiducial values of $p = 2.4$ and $\epsilon_B = 10^{-2}$. We also re-analyze GRB 050724A, first presented in Fong et al. (2016b), using the appropriate values for ϵ_B and n_0.

The fixed $E_{\rm ej}$–n_0 grid is defined by 250 log-spaced points in each parameter, with the ranges $E_{\rm ej} = 10^{50}$–10^{54} erg and $n_0 = 10^{-6}$–10^{2} cm^{-3}. The minimum and maximum circumburst densities are chosen to represent the extremes in which short GRBs are expected to occur, from a low value for the intergalactic medium particle densities to those of star-forming regions. We note that the median density of short GRBs, commensurate with their kicked progenitors, is $n_0 \approx 10^{-3}$–10^{-2} cm^{-3} (Fong et al. 2015).

To translate these models to an $E_{\rm ej} - n_0$ parameter space, for each model we calculate the value of F_ν at the rest-frame time of observation ($\delta t_{\rm rest}$). This flux mapping is displayed as a gray-scale gradient in Figure 2. We also determine the corresponding solution (solid purple line) represented by the measured limit, where the parameter space below each limit is allowed while parameter space above each limit is ruled out (Figure 2). Notably, most of the solutions corresponding to the low-redshift events can rule out parameter space below the 10^{53} erg maximum energy for a wide range of densities. For a direct comparison, we derive the same solution using the analytical models from Nakar & Piran (2011), shown as a black dashed line. As expected, our models deviate significantly from the analytical solutions in the high-energy, low-density parameter space when relativistic effects are expected to be strongest (see also, Liu et al. 2020).

We determine the upper limit on the energy for each burst ($E_{\rm ej,max}$), by imposing a density prior and fixing the densities to those derived from the broadband afterglow (Section 4.2; Table 2).

The values of $E_{\rm ej,max}$ for the 10 bursts for both ejecta mass scenarios are shown in Figure 2 and also listed in Table 2. Finally, motivated by the fact that we do not know the true value of ϵ_B, and this in turn has an effect on the inferred maximum energies, we calculate solutions in the $E_{\rm ej}$–n_0 parameter space for $\epsilon_B = 10^{-1}$ and $\epsilon_B = 10^{-4}$ (see Liu et al. 2020 for an in-depth exploration of the dependence on ϵ_B). Decreasing ϵ_B overall weakens the constraints on the parameter space (Figure 3). However, a lower value of ϵ_B also results in an increase in the inferred circumburst density (Granot & Sari 2002). Conversely, increasing ϵ_B overall strengthens the constraints on the parameter space and results in a decrease in the inferred circumburst density. The end result is a slight decrease in the values of $E_{\rm ej,max}$: for instance, for GRB 130603B a factor of 10 increase from $\epsilon_B = 10^{-2}$ to $\epsilon_B = 10^{-1}$ results in a decrease in the ejecta energy limit by a factor of ≈1.7 ($E_{\rm ej,max} = 1.10 \times 10^{52}$ erg to 0.65×10^{52} erg for $M_{\rm ej} = 0.03\,M_\odot$).

To constrain the fastest ejecta deposited by a magnetar remnant in the BNS merger GW170817 (Abbott et al. 2017b), we perform the same analysis to create an $E - n_0$ parameter space. We use the median of the physical parameters determined by Hajela et al. (2019) of $p = 2.15$, $\epsilon_e = 0.18$, and $\epsilon_B = 0.0023$ (see also: Makhathini et al. 2020). We set the ejecta mass to be $M = 0.05 M_\odot$ (Villar et al. 2017; Arcavi 2018). This flux mapping is displayed as gray-scaled gradient in Figure 4. We also determine the corresponding solution (solid purple line) represented by the measured 3σ limit at $\delta t_{\rm rest} \approx 2$ yr of $F_\nu < 8.4$ μJy (Hajela et al. 2019). We determine the upper limit on the energy for GW170817 by imposing a density prior and fixing the density to 2.5×10^{-3} cm^{-3}. We find a value of $E_{\rm ej,max} = 1.32 \times 10^{52}$ erg (Figure 4).

Finally, we compute the probability distribution function (PDF) of ejecta energies for each burst, with and without the circumburst density prior. We note that without the density prior, the shape of each distribution is mainly governed by our choice of density grid and the flux upper limit, overall resulting in lower values of $E_{\rm ej,max}$ (Figure 5). We show both distributions for completeness, as we assumed a fiducial density range for ~1/3 of the sample; however, the following results are based on use of the density priors. In this analysis, we include 18 additional bursts with 5.5 and 6.0 GHz observations from the literature (Fong et al. 2016b; Klose et al. 2019),

Table 2
Short GRB Afterglow and Neutron-star Remnant Properties

GRB	z	n_0 (cm^{-3})	p	ε_B	$E_{\mathrm{ej,max}}$ ($0.03\,M_\odot$) (10^{52} erg)	$E_{\mathrm{ej,max}}$ ($0.1\,M_\odot$) (10^{52} erg)
This work						
GRB 050509B	0.225	<0.55	2.52	10^{-2}	0.73–17.58[a]	0.79–39.66[a]
GRB 060502B	0.287	0.01	2.4	10^{-2}	1.59	2.98
GRB 100206A	0.41	0.01	2.4	10^{-2}	2.06	4.64
GRB 130603B	0.356	$0.31^{+0.08}_{-0.04}$	2.7	10^{-2}	1.1	1.98
GRB 130822A	0.154	0.01	2.4	10^{-2}	1.02	3.09
GRB 140903A	0.351	$3.40^{+2.9}_{-1.6} \times 10^{-3}$	2.27	10^{-3}	6.72	14.08
GRB 150120A	0.46	0.01	2.4	10^{-2}	2.13	6.24
GRB 150424A	0.3	$1.98^{+4.4}_{-1.4} \times 10^{-4}$	2.4	10^{-2}	5.58[b]	17.58[b]
GRB 160821B	0.16	$0.13^{+0.05}_{-0.04}$	2.36	10^{-2}	0.56	1.77
Fong et al. (2016b)						
GRB 050724A	0.257	$0.89^{+0.58}_{-0.49}$	2.29	10^{-4}	5.79	6.01
GRB 051221A	0.546	$0.14^{+0.05}_{-0.04}$	2.24	10^{-2}	2.06	2.87
GRB 070724A	0.457	$9.30^{+210.0}_{-9.2} \times 10^{-5}$	2.24	10^{-2}	11.28	25.45
GRB 080905A	0.122	$7.10^{+610.0}_{-7.1} \times 10^{-4}$	2.06	10^{-2}	2.87	8.08
GRB 090510	0.903	$6.40^{+100.0}_{-6.0} \times 10^{-5}$	2.65	10^{-2}	25.45	47.72
GRB 090515	0.403	0.01	2.4	10^{-2}	2.87	6.72
GRB 100117A	0.915	$1.2^{+0.9}_{-0.3}$	2.36	10^{-2}	2.06	2.98
GRB 101219A	0.718	$2.40^{+97.0}_{-2.3} \times 10^{-4}$	2.73	10^{-2}	11.7	28.43
Klose et al. (2019)						
GRB 061006	0.438	$1.20^{+29.0}_{-1.1} \times 10^{-4}$	2.39	10^{-2}	13.08	27.4
GRB 061201	0.111	$2.70^{+120.0}_{-2.6} \times 10^{-4}$	2.35	10^{-2}	3.33	9.73
GRB 061210A	0.41	0.01	2.4	10^{-2}	3.45	6.48
GRB 070729	0.8	0.01	2.4	10^{-2}	8.39	12.6
GRB 070809	0.219	$1.20^{+30.0}_{-1.1} \times 10^{-4}$	2.12	10^{-2}	7.23	18.93
GRB 080123	0.496	0.01	2.4	10^{-2}	3.86	8.39
GRB 090621B	0.5[c]	$1.0^{+0.52}_{-0.27}$	2.64	10^{-2}	2.06	2.39
GRB 100816A	0.805	0.01	2.4	10^{-2}	2.87	8.39
GRB 101224A	0.454	0.01	2.4	10^{-2}	3.45	8.39
GRB 130515A	0.5[c]	0.01	2.4	10^{-2}	3.86	11.28

Notes. Upper limits, $E_{\mathrm{ej,max}}$ calculated for two ejecta masses, $M_{\mathrm{ej}} = 0.03\,M_\odot$ and $M_{\mathrm{ej}} = 0.1\,M_\odot$, at the median inferred density inferred from the afterglow. If afterglow constraints do not exist, we use fiducial values, $p = 2.4$, $n = 0.01$ cm^{-3}, $\epsilon_e = 0.1$, and $\epsilon_B = 10^{-2}$.
[a] Range is quoted corresponding to $n_0 = 10^{-6} - 0.55$ cm^{-3} where the upper bound is set by the afterglow parameters.
[b] We note that if we assume $z = 1$ for GRB 150424A, the values for $E_{\mathrm{ej,max}} = 11.70$ (for $0.03\,M_\odot$) and $E_{\mathrm{ej,max}} = 31.77$ (for $0.1\,M_\odot$).
[c] Redshift is set to a fiducial value of 0.5 for GRBs with no known redshift.

representing the full available sample of meaningful observations at these frequencies. We use spectroscopic redshifts for all events except for two for which we assume $z = 0.5$ (the median of the short GRB population; Fong et al. 2017). We present a revised redshift for GRB 101224A of $z = 0.454$ based on spectroscopy obtained with the Large Binocular Telescope (LBT; PI Fong), which we use in this analysis. We combine the PDFs and normalize the area under the PDF to unity, to create cumulative distribution functions (CDFs), shown in Figure 5.

5. Short GRB Constraints on M_{TOV}

5.1. Predictions for Energy Output for Varying M_{TOV}

We now compare the constraints on the maximum energy deposited from NS remnants to theoretical expectations. The characteristic energy scale of kilonovae ejecta without additional magnetar energy deposition is $E_{\mathrm{ej}} \lesssim 10^{50.5}$ erg. The rotational energy of a post-merger remnant magnetar can reach $\sim 10^{53}$ erg. If an NS remnant remains stable for sufficiently long timescales following merger ($\gtrsim$viscous timescale $\sim$0.1–1 s), it can deposit a large fraction of this rotational energy into the kilonova ejecta through magnetic-dipole spin-down. Whether or not the merger remnant remains stable long enough for this to take place depends sensitively on the total mass of the binary and M_{TOV}. The mass of merging binary NSs is measurable for mergers detected by LIGO, however is inaccessible based on short GRB observations alone. Thus, predictions for the energy of merger ejecta associated with short GRBs depend on the assumed mass distribution of BNS mergers and the uncertain value of M_{TOV}.

In Figure 5 we compare the probability distribution of maximum energy $E_{\mathrm{ej,max}}$ obtained from our radio upper limits (purple) to model-predicted probability distributions of E_{ej} (gray) created following Margalit & Metzger (2019). We assume the cosmological population of BNS mergers follows the Galactic double NS distribution (Kiziltan et al. 2013). We

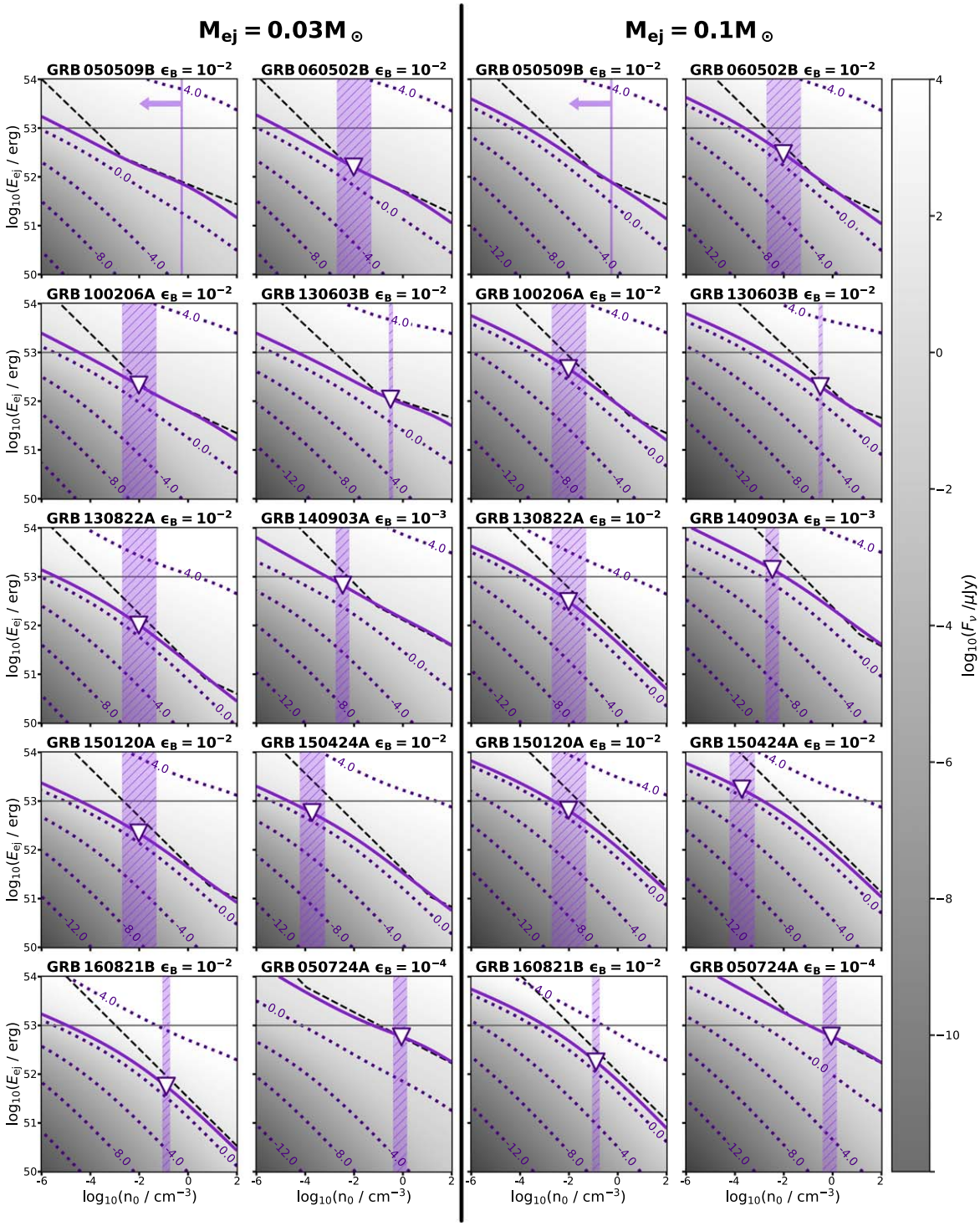

Figure 2. Ejecta energy E_{ej} vs. circumburst density n_0 parameter space for 10 short GRBs (nine in this work, and GRB 050724A from Fong et al. 2016b) for two ejecta masses, $M_{ej} = 0.03M_\odot$ (left) and $M_{ej} = 0.1M_\odot$ (right). The solution for each GRB is shown (purple solid line), in which parameter space above the line is ruled out and parameter space below the line is allowed. Also shown is the flux density solution for each GRB at the rest-frame time of the observation (gray-scale map) and contours (indigo dotted lines) that are spaced by 10^4 μJy. The purple shaded region corresponds to the density constraints used from afterglow measurements, with a fiducial range of $n_0 = (0.2\text{–}5) \times 10^{-2}$ cm^{-3} if no constraint is available. The triangle in each frame is the upper limit placed on E_{ej} at the median density. A comparison to the analytical model solution (black dashed line; Nakar & Piran 2011) demonstrates that the largest deviations are for high values of E_{ej} and low values of n_0. A gray horizontal line at 10^{53} erg denotes the maximum extractable energy expected for a stable magnetar with $M \sim 2.2M_\odot$.

then draw random NS masses from this distribution and estimate the ejecta mass and velocity for each pair $\{m_1, m_2\}$ based on fitting formulae to numerical-relativity simulations (Coughlin et al. 2018). In addition to the dynamical ejecta, we add a disk-wind ejecta component whose velocity is taken as $0.15c$ and whose mass is taken to be a fraction 0.4 of the disk mass (Siegel & Metzger 2017), estimated from Coughlin et al. (2019; see also Radice et al. 2018). In the above we adopt an

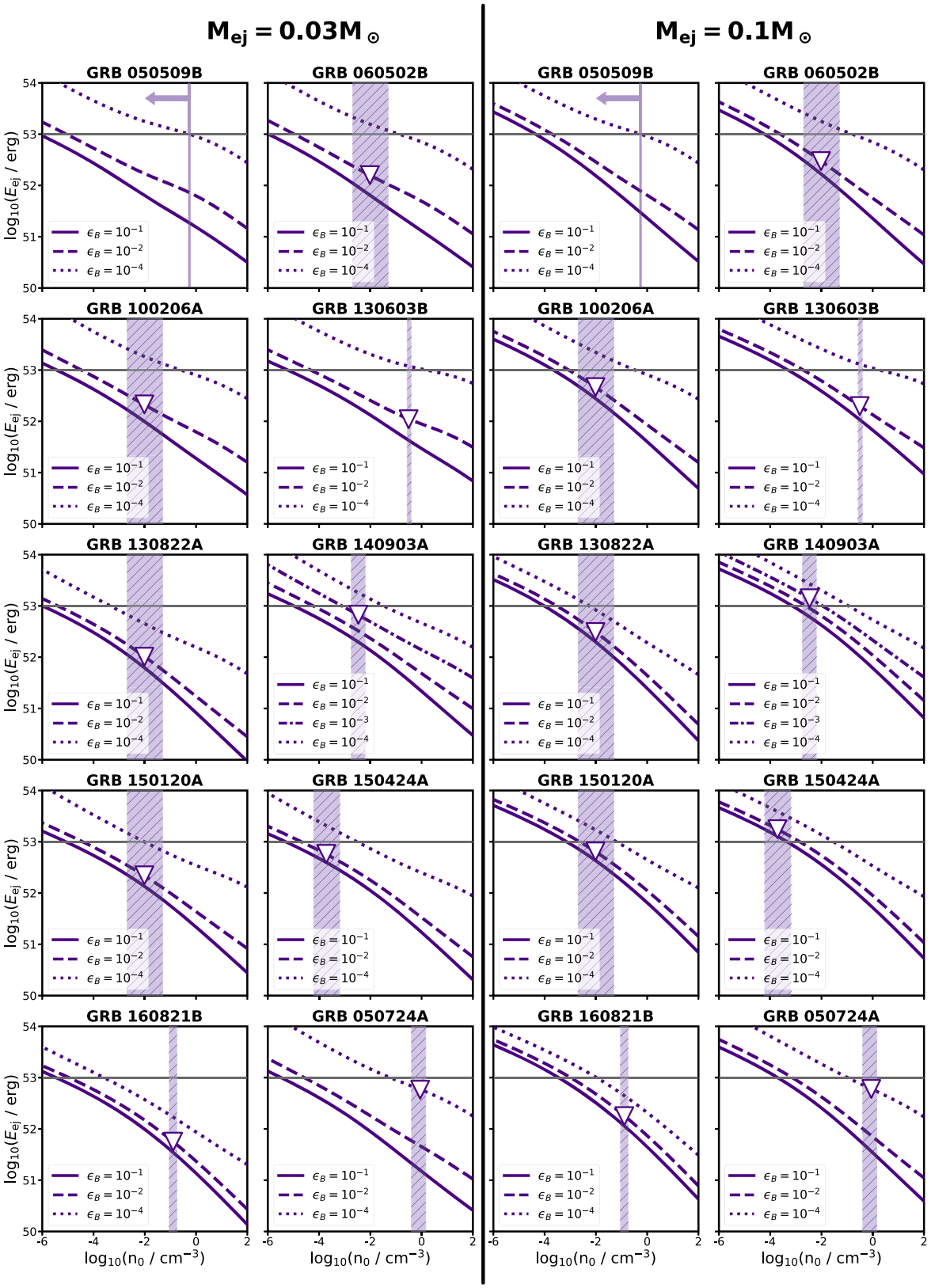

Figure 3. Ejecta energy E_{ej} vs. circumburst density n_0 parameter space for 10 short GRBs for two ejecta masses, $M_{ej} = 0.03M_\odot$ (left) and $M_{ej} = 0.1M_\odot$ (right). Curves represent limits for three values of $\epsilon_B = 10^{-1}$, 10^{-2} (fiducial), and 10^{-4}, except in the case of GRB 140903A in which the additional line represents the best-fit $\epsilon_B = 10^{-3}$. The purple shaded regions correspond to the density constraints from the afterglow, or the fiducial range if no constraints were found. Triangles correspond to the value of $E_{ej,max}$ of the median density inferred for the fiducial value of $\epsilon_B = 10^{-2}$, except in the cases of GRB 140903A ($\epsilon_B = 10^{-3}$) and GRB 050724A ($\epsilon_B = 10^{-4}$). A gray horizontal line at 10^{53} erg denotes the maximum extractable energy expected for a stable magnetar with $M \sim 2.2M_\odot$.

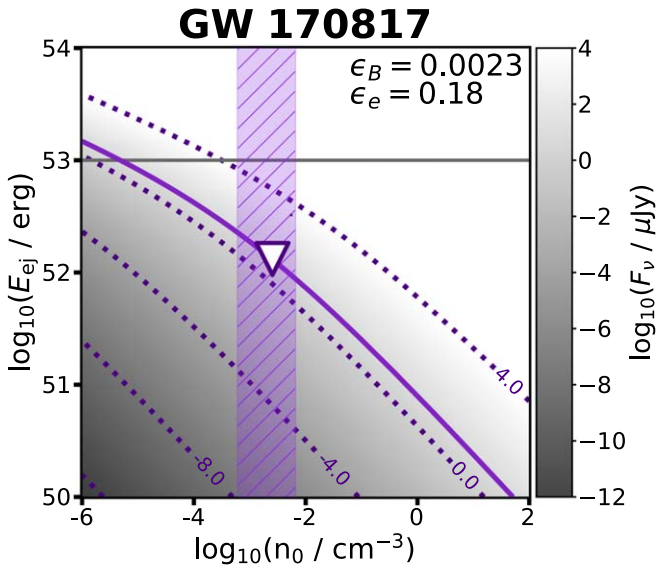

Figure 4. Ejecta energy E_{ej} vs. circumburst density n_0 parameter space for GW170817 for ejecta mass $M_{ej} = 0.05M_\odot$ and microphysical parameters $\epsilon_e = 0.18$ and $\epsilon_B = 0.0023$, found by Hajela et al. (2019). The solution for GW170817 is shown (purple solid line), in which parameter space above the line is ruled out and parameter space below the line is allowed. Also shown is the flux density solution for GW170817 at the rest-frame time of the observation (gray-scale map), and contours (indigo dotted lines) spaced by 10^4 μJy. The purple shaded region corresponds to the density constraints used from afterglow measurements. A gray horizontal line at 10^{53} erg denotes the maximum extractable energy expected for a stable magnetar with $M \sim 2.2M_\odot$.

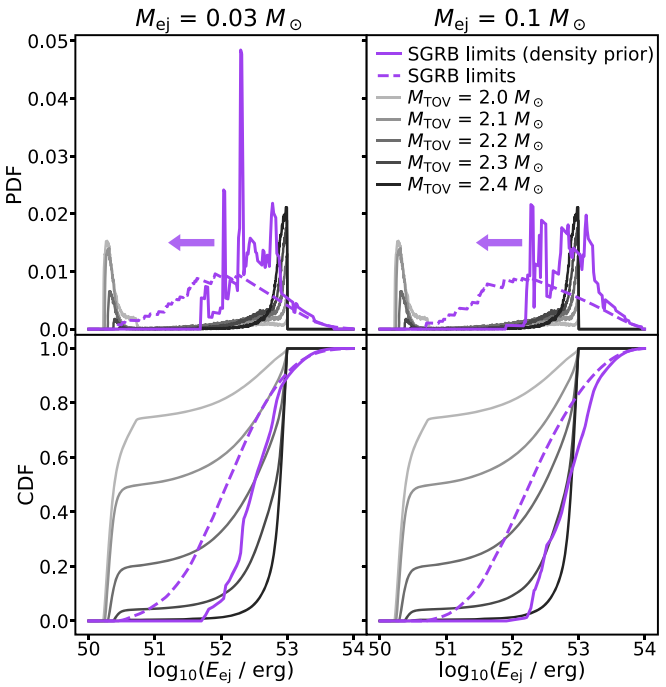

Figure 5. Top: PDFs for the upper limits on the kinetic energies, E_{ej}, allowed by radio observations of 27 short GRBs for ejecta masses of $M_{ej} = 0.03\,M_\odot$ (left) and $0.1\,M_\odot$ (right). PDFs represent an "upper limit" distribution and are shown for the sample with no density prior (dashed purple lines), in which case the shape of the distribution is mainly controlled by the choice of density grid and flux upper limits (including the density prior; solid purple lines). Also shown are predictions for a range of $M_{TOV} = 2.0$–$2.4\,M_\odot$ (gray-scale lines). Bottom: CDFs for the observed and predicted distributions.

NS radius of 11 km (Capano et al. 2020), but our results are not particularly sensitive to this choice.

The procedure above defines a PDF of kilonova ejecta energy lacking any additional magnetar energy deposition. Such energy deposition is then taken into account as a function of the merger remnant mass ($M^b_{rem} = m^b_1 + m^b_2 - M^b_{ej}$, where superscript "b" denotes baryonic mass) with respect to M_{TOV}. We approximate this function as $T = T_{max}\,(M^b_{rem}/M^b_{TOV})^\alpha$ for $M^b_{rem} \leqslant M^b_{TOV}$ and $T = T_{max}\,[(\xi - M^b_{rem}/M^b_{TOV})/(\xi - 1)]^\beta$ for $M^b_{rem} > M^b_{TOV}$, with $T_{max} = 10^{53}$ erg, $\xi = 1.18$, $\alpha = 2.35$, and $\beta = 1.3$. These parameters were found to reasonably approximate the extractable magnetar rotational energy for a range of EOS tested with the RNS code (Stergioulas & Friedman 1995), and ensure that $T = 0$ (no magnetar energy deposition) for an NS that collapses before reaching solid-body rotation ($M^b_{rm} \gtrsim \xi M^b_{TOV}$). For systems with long-lived magnetar remnants, we add the extractable rotational energy T to the total kilonova ejecta energy, essentially assuming an efficiency $\zeta = 1$ for this energy deposition process. As illustrated in Figure 5, the resulting predicted distributions for all values of M_{TOV} are bimodal, with $E_{ej} > 10^{52.5}$ erg, representing "long-lived" remnants with magnetar energy deposition and $E_{ej} \lesssim 10^{50.5}$ erg representing "normal" kilonova ejecta energies (without a magnetar energy boost). We note that these E_{ej} model predictions do not depend on radiation physics nor in particular on the microphysical parameters ϵ_e, ϵ_B, p, and ζ_e.

For $M_{ej} = 0.03\,M_\odot$, the majority of the observational energy constraints are concentrated in the region $E_{ej} \approx 10^{51.5} - 10^{53.5}$, with a median upper limit of $\approx 10^{52.5}$ erg. A basic comparison of the existing short GRB limits to expectations demonstrates that we can rule out the majority of $M_{TOV} = 2.3$–$2.4\,M_\odot$ models for $M_{ej} = 0.03\,M_\odot$. Moreover, the limits rule out the maximum expected energy outputs for $M_{TOV} = 2.2\,M_\odot$ and $2.3\,M_\odot$ models. The limits are less stringent in the case of $M_{ej} = 0.1\,M_\odot$; however in this regime we can still rule out the majority of the $2.4\,M_\odot$ model.

5.2. The Role of High-mass BNS Mergers

A major assumption in the estimates of the previous subsection is that short GRBs are produced exclusively by BNS mergers that track the Galactic double NS mass distribution. The recent detection of GW190425 by the LIGO and Virgo GW detectors (Abbott et al. 2020) is a clear counter-example to this assumption, as its total mass is 5σ above the mean Galactic NS binary population (though there is no observational proof that GW190425-like events produce short GRBs). If a large fraction of mergers involve high-mass systems akin to GW190425, then the constraints on M_{TOV} would be weakened. This is due to the fact that only mergers with a total mass $\lesssim \xi\,M_{TOV}$ can produce long-lived magnetar remnants capable of enhancing the ejecta energy. The effect would be similar if a large fraction of short GRBs originated from NS–BH mergers (e.g., Gompertz et al. 2020).

To investigate this in a more quantitative way, we add a population of "high-mass," GW190425-like BNS systems to our analysis. We take the mass of these systems to be $m_1 = m_2 = 1.65M_\odot$ motivated by GW190425 (Abbott et al. 2020), and parameterize the fractional contribution of this high-mass population to the total BNS population as $f_{GW190425}$. This is similar to the approach recently adopted by Sarin et al. (2020). In this notation, $f_{GW190425} = 0$ corresponds to a purely Galactic double NS mass distribution, while $f_{GW190425} = 1$

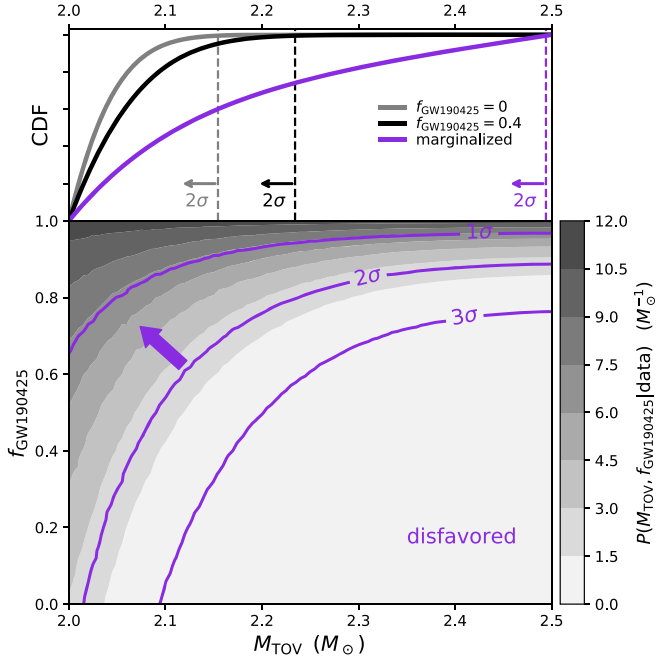

Figure 6. Bottom: joint PDF of the NS maximum mass, $M_{\rm TOV}$, and the fractional contribution $f_{\rm GW190425}$ of "high-mass" systems to the total population of BNS mergers (the remainder, $1 - f_{\rm GW190425}$, of which is assumed to follow the Galactic BNS mass distribution). Mergers whose total mass is $\lesssim \xi M_{\rm TOV} \approx 1.2 M_{\rm TOV}$ are predicted to form "long-lived" magnetar remnants that would deposit a large amount of energy into the surrounding kilonova ejecta, a scenario that can be constrained by our radio observations (Table 2; Figure 2). Our radio upper limits can be reconciled with these predictions if few mergers produce long-lived magnetar remnants, implying small $M_{\rm TOV}$ and/or moderate to large values for $f_{\rm GW190425}$ (purple contours, bottom panel). Top: cumulative $M_{\rm TOV}$ distribution function for $f_{\rm GW190425} = 0$ (gray), $f_{\rm GW190425} = 0.4$ (black), and marginalized over $f_{\rm GW190425}$ (purple). The 2σ (statistical) upper limits on $M_{\rm TOV}$ are marked with vertical dashed curves, from which we find $M_{\rm TOV} \lesssim 2.15\ M_\odot$ ($2.23\ M_\odot$) for $f_{\rm GW190425} = 0$ (0.4).

corresponds to one with only high-mass GW190425-like systems (clearly at odds with GW170817). We then perform a series of calculations for a grid of $M_{\rm TOV}$ and $f_{\rm GW190425}$ values: for each set of parameters, we produce a model CDF for $E_{\rm ej}$ (as in Figure 5, but with the addition of the high-mass GW190425-like population); the conditional probability of the model parameters given the data ($E_{\rm ej}$ upper limits summarized in Table 2) is then calculated as

$$P(M_{\rm TOV}, f|{\rm data}) = \frac{P({\rm data}|M_{\rm TOV}, f)}{\int\int P({\rm data}|M'_{\rm TOV}, f')\, dM'_{\rm TOV}\, df'}, \quad (2)$$

where

$$P({\rm data}|M_{\rm TOV}, f) = \prod_i P(E_{\rm ej} < E^{(i)}_{\rm ej,max}|\ M_{\rm TOV}, f), \quad (3)$$

and we have introduced the shorthand notation $f \equiv f_{\rm GW190425}$. Equation (2) implicitly assumes a uniform prior $P(M_{\rm TOV}, f) =$ constant. Finally, the index i runs over all sources in Table 2, and the term $P(E_{\rm ej} < E^{(i)}_{\rm ej,max}|M_{\rm TOV}, f)$ in Equation (3) is calculated using the model CDFs.

Figure 6 shows the joint constraints on the $M_{\rm TOV}$–$f_{\rm GW190425}$ parameter space, calculated using the $M_{\rm ej} = 0.1 M_\odot$ limits in Table 2. The PDF $P(M_{\rm TOV}, f|{\rm data})$ is plotted in the bottom panel, where purple contours demarcate the region to the left of which 1σ, 2σ, and 3σ of the cumulative probability is contained. As discussed above, the constraints on $M_{\rm TOV}$ are reduced for a larger fraction of high-mass mergers (large $f_{\rm GW190425}$) because such mergers do not form long-lived magnetars that can enhance the kilonova ejecta energy to $\gtrsim 10^{52}$ erg, comparable to our radio limits. The top panel of Figure 6 shows the marginalized $M_{\rm TOV}$ CDF (purple), in addition to the CDF at fixed $f_{\rm GW190425} = 0$ (gray) and $f_{\rm GW190425} = 0.4$ (black). The 2σ upper limits[11] on $M_{\rm TOV}$ based on these CDFs are plotted with corresponding vertical dashed curves. For $f_{\rm GW190425} = 0$ the limits implied by the model necessitate $M_{\rm TOV} \lesssim 2.15 M_\odot$. This is slightly deeper than other current limits on $M_{\rm TOV}$, which is constrained by massive-pulsar observations to $M_{\rm TOV} \gtrsim 2.0 M_\odot$ (Demorest et al. 2010; Antoniadis et al. 2013; Cromartie et al. 2020) and by observations of GW170817 to $M_{\rm TOV} \lesssim 2.2$–$2.3 M_\odot$ (Margalit & Metzger 2017; Shibata et al. 2019). However, larger values of $f_{\rm GW190425}$ relax this $M_{\rm TOV}$ constraint. The ratio between the median total LIGO-inferred rate of BNS mergers and the median rate of BNS mergers akin to GW190425 ($\mathcal{R}_{\rm GW190425}$) suggests $f_{\rm GW190425} \sim 0.4$, albeit with large uncertainties given the small sample size (Abbott et al. 2020). For this value of $f_{\rm GW190425} = 0.4$, we find $M_{\rm TOV} \lesssim 2.23 M_\odot$. Larger values of $f_{\rm GW190425}$ would further weaken our constraint. Indeed, marginalized over $f_{\rm GW190425}$, we find unconstraining limits on $M_{\rm TOV}$.

Compared to direct pulsar-mass measurements or even multi-messenger constraints from GW170817, the methodology we have developed here for constraining $M_{\rm TOV}$ is far more sensitive to various systematic uncertainties. This method is statistical in nature and relies on a description of the a priori unknown mass distribution of merging NSs (e.g., Lawrence et al. 2015; and see, e.g., Lasky et al. 2014 for an analogous methodology in the context of the magnetar-model for short GRB X-ray plateaus). Here we have assumed that this distribution is a mixture of the observed Galactic double NS distribution and a population of GW190425-like events governed by a single free parameter $f_{\rm GW190425}$; however the true mass distribution can in principle differ significantly from this assumption. Future GW detections will shed light on the local-universe population of merging NSs and can be used to improve this methodology in the future.

The parameterization of the kilonova ejecta energy $E_{\rm ej}$ as a function of binary parameters, and in particular the universal form of magnetar energy deposition T that we adopt, can also quantitatively influence our upper limits on $M_{\rm TOV}$ (as can assumptions about the ejecta mass, though we have here adopted a conservative (large) value of $M_{\rm ej} = 0.1 M_\odot$).

Finally, the efficiency ζ of coupling between the magnetar spin-down energy and the energy deposited into the ejecta (here assumed to be $\zeta = 1$) can also impact our results, as can a more conservative (lower) value of ϵ_B. If $\zeta < 1$ and the remainder $(1 - \zeta)$ of the spin-down energy is emitted as an ultra-relativistic pulsar wind, this would amount to depositing some fraction of the energy into even higher-velocity material leading to more luminous light curves and stronger constraints on magnetar formation. This is a consequence of the fact that the early ($t < t_{\rm dec}$) light curve scales strongly with outflow velocity (at late times, the light curve depends only on the total outflow energy and is thus independent of ζ). Only in a scenario where $1 - \zeta$ of the spin-down energy is instead radiated "silently" through GW losses would our derived constraints be weakened. However this scenario requires an

[11] This corresponds to the statistical significance, and does not include possible systematics.

unusually large NS ellipticity or extremely low external dipole field (Ai et al. 2018), which is not expected (e.g., Kiuchi et al. 2014). Systematics in the numerical-relativity fitting formulae and approximate magnetar rotational-energy curve we have adopted can also impact our results, though the former do not have much effect on the high-$E_{\rm ej}$ distribution most relevant for this study.

6. Observational Prospects in Constraining BNS Remnants

For our low-redshift sample, we find maximum ejecta energies of $E_{\rm ej,max} = (0.6–6.7) \times 10^{52}$ erg for an ejecta mass of $0.03 M_\odot$ and $E_{\rm ej,max} = (1.8–17.6) \times 10^{52}$ erg for $0.1 M_\odot$. This excludes GRB 050509B for which there is only a density upper limit, and thus we calculate a wide range of $E_{\rm ej,max} \approx (0.7–39.7) \times 10^{52}$ erg for that burst. This work provides a re-analysis of seven short GRB observations presented in Fong et al. (2016b), and supercedes that analysis. The effects of more well-motivated assumptions on the value of ϵ_B, combined with our new models, which include relativistic effects, overall result in deeper constraints on $E_{\rm ej,max}$ by factors of ≈2–12 for most of these events. For GRB 090515, we provide a new analysis based on a fiducial density, and for GRB 130603B, we use both of the observations presented here and in Fong et al. (2016b) and take the more constraining of the two solutions. We use the 5.5 GHz VLA and ATCA limits from Klose et al. (2019), who were searching for optically obscured star formation in their host galaxies, for an additional 10 GRBs and find $E_{\rm ej,max} = (2.1–13.1) \times 10^{52}$ erg for $M_{\rm ej} = 0.03 M_\odot$ and $(2.5–27.4) \times 10^{52}$ erg for $M_{\rm ej} = 0.1 M_\odot$. Our light-curve model is nearly identical to that presented by Liu et al. (2020). Our modeling overall provides more constraining limits on ejecta energies than studies that used the analytic approximation (Nakar & Piran 2011), and the models primarily differ in their pre-peak behavior. The claim by Liu et al. (2020) that their model is significantly less constraining at late times than Fong et al. (2016b) appears to be due to assumptions they make about the analytic model. In summary, the constraints on ejecta energies here are significantly deeper than those of any previous study on short GRBs.

Going forward, there are three primary observational avenues to place constraints on the nature of the remnants produced in BNS mergers: (i) continued observations of cosmological short GRBs, (ii) follow-up of GW events, and (iii) searches in untargeted radio surveys, such as the Very Large Array Sky Survey (VLASS; Lacy et al. 2020). We briefly explore prospects for each of these avenues here.

Our low-redshift sample has demonstrated that for $z \lesssim 0.5$, current deep VLA observations that reach depths of $F_\nu \approx$ 10–20 μJy can achieve limits of $E_{\rm ej,max} \approx 10^{52}$ erg, ruling out indefinitely stable remnants, and potentially some supramassive remnants. As demonstrated in Figure 5, the predicted energy distribution is bimodal, with a low-energy peak at $E_{\rm ej} < 10^{51}$ erg corresponding to kilonovae ejecta whose energy is not enhanced by magnetar energy deposition. In these cases, the peak flux density is $F_\nu \lesssim$ 0.1–1 μJy at ∼GHz frequencies (for $z = 0.1–0.4$), infeasible with current or planned radio facilities. Thus, while continued follow-up of short GRBs is an effective way to place limits of $E_{\rm ej} \approx 10^{52}$ erg, it is not possible to constrain energies well below these values from the cosmological short GRB population.

The remnants of short GRBs can in principle be constrained by observations at gamma-ray and X-ray wavelengths. For instance, anomalous X-ray behavior that deviates from the standard GRB model, such as extended emission extending tens to hundreds of seconds in gamma-ray light curves (Bucciantini et al. 2012; Gompertz et al. 2013; Murase et al. 2018), X-ray plateaus (Rowlinson et al. 2013; Lü et al. 2015; Stratta et al. 2018), and late-time X-ray excess emission on timescales of $\gtrsim$1 day (Perley et al. 2012; Fong et al. 2014) can all be interpreted as energy injection from long-lived magnetar remnants. Under this assumption, they can be analogously used to constrain $M_{\rm TOV}$ (e.g., Fan et al. 2013; Lasky et al. 2014; Gao et al. 2016; Sarin et al. 2020). The inferred magnetar energies from these injection sources are consistent with or slightly lower than those inferred from radio limits, with $\approx(0.3–5) \times 10^{52}$ erg. Among the current sample with radio observations, 13 events have anomalous X-ray behavior (Rowlinson et al. 2013; Lü et al. 2015; Fong et al. 2016b; Lien et al. 2016), and seven of these have constraints well below the extractable energy from a stable remnant of $E_{\rm ej,max} < 10^{53}$ erg (Table 2). For these bursts, the inferred maximum energies from radio observations are comparable to the inferred injection energies from the X-ray band.

We can use the short GRB population to quantify the fraction of indefinitely stable magnetar remnants (e.g., those that can effectively transfer 10^{53} erg of energy to the environment), $f_{\rm stable}$. The sample presented here covers Swift short GRBs discovered from 2005–2016, out of a total detected 115 events (including 12 short GRBs with extended emission; Lien et al. 2016). For $M_{\rm ej} = 0.03\,M_\odot$, we derive $E_{\rm ej,max} < 10^{53}$ erg (corresponding to the maximum energy deposited by an indefinitely stable magnetar with $M \lesssim M_{\rm TOV}$) for 22 short GRBs, or 19% of the total Swift short GRB population. Thus, we place a limit of $f_{\rm stable} < 0.81$.

To date, every short GRB with radio follow-up observations on the relevant timescales has yielded non-detections, and the large majority have limits of $E_{\rm ej,max} < 10^{53}$ erg (Table 2). In particular, if the low-redshift ($z < 0.5$) subset of short GRBs is representative of the entire short GRB population in terms of the nature of the remnant, and there is no redshift dependence in remnant stability once a short GRB is produced, we can use this population to place a stronger constraint on the value of $f_{\rm stable}$. Of the 25 short GRBs at $z < 0.5$, 19 have radio observations on the relevant timescales, while 13 events have $E_{\rm ej,max} < 10^{53}$ erg, ruling out a stable remnant (Table 2). Thus, we employ an additional constraint from the low-redshift short GRB population of $f_{\rm stable} < 0.48$ (Figure 7); this means that the majority of short GRBs do not produce stable remnants. This agrees with theoretical expectations (e.g., Margalit & Metzger 2019; see also Piro et al. 2017), although the exact requirements for post-merger product to form a disk and launch a GRB jet, as well as how this connects to the nature of the remnant, is still an open question (e.g., Margalit et al. 2015; Ruiz & Shapiro 2017; Mösta et al. 2020).

This calculation assumes that BNS mergers are the progenitors of all short GRBs. If, for instance, NS–BH mergers contribute significantly to the short GRB population (Gompertz et al. 2020), the constraints on $f_{\rm stable}$ are weakened. Current volumetric rate estimates of NS–BH mergers are uncertain: a comparison of the upper limit on the rate of NS–BH mergers from GW facilities (LIGO Scientific Collaboration & Virgo Collaboration 2019) and the value measured from short GRBs (Fong et al. 2015) demonstrates that current GW observations can accommodate any fraction of short GRBs produced by NS–BH mergers. Meanwhile, population synthesis studies result in rates that are comparable to (e.g., Eldridge et al. 2019) or considerably lower than (Belczynski et al. 2020) the NS–NS merger population. The

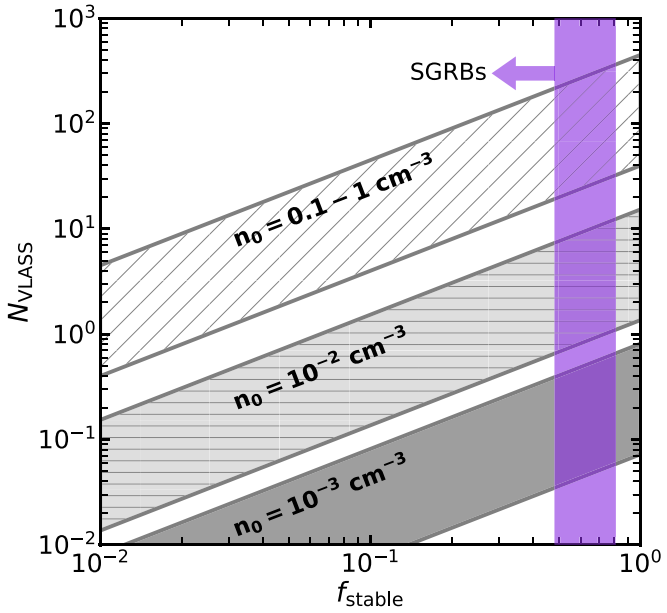

Figure 7. The number of radio magnetar remnants detectable at the level of 10σ in a VLASS epoch ($N_{\rm VLASS}$; $\sigma_{\rm rms} = 120\ \mu$Jy) vs. the fraction of stable remnants in the BNS merger population ($f_{\rm stable}$). Characteristic numbers are calculated for a stable remnant, which deposits $E_{\rm ej} = 10^{53}$ erg in the surrounding medium for varying densities ($n_0 = 10^{-3} - 1$ cm^{-3}). The gray shaded and hatched regions for each density correspond to the uncertainty in the BNS merger rate (Abbott et al. 2020). The purple shaded region corresponds to the range of $f_{\rm stable}$ determined by short GRBs. We note that $N_{\rm VLASS}$ corresponds to the detectability of radio remnants but does not include the contamination and uncertainties introduced by the proper identification of slowly evolving radio transients as radio remnants.

parameter space in which a typical $1.4\,M_\odot$ NS can be disrupted by a BH to produce an observable EM counterpart is extremely limited (Foucart 2012; Capano et al. 2020; e.g., low-mass and high-spin), and it is unlikely that NS–BH mergers are the majority progenitor population for short GRBs.

A second avenue to constrain the nature of the remnant is by more local GW events. Their proximity enables potentially deep constraints on the value of $E_{\rm ej,max}$ via EM observations or GWs (e.g., Murase et al. 2018), although this is also dependent on the values of the microphysical parameters; in particular, low values of ϵ_B weaken the constraints (e.g., Figure 3; Liu et al. 2020). Indeed, GW170817 has a low inferred value of $\epsilon_B = 0.0023$ (Hajela et al. 2019); from these, we infer $E_{\rm ej,max} = 1.3 \times 10^{52}$ erg for the fast kilonova ejecta (Figure 4). Several studies based on broadband afterglow, and in particular X-ray observations of GW170817, were able to rule out a long-lived stable or supramassive remnant (e.g., Margalit & Metzger 2017; Shibata et al. 2017; Margutti et al. 2018; Pooley et al. 2018). It has been argued that GW170817 produced a temporarily stable hypermassive NS (Margalit & Metzger 2017) and that this millisecond magnetar could explain the high ejecta mass, high velocity, and high electron fraction (Metzger et al. 2018). If the rate of low-mass BNS mergers (less massive than GW170817) is less than the rate of GW170817-like events, then a weak upper limit on $f_{\rm stable}$ also comes from the relative rates of GW170817-like events with respect to the total BNS merger rate (e.g., $f_{\rm stable} < 0.6$) but with large uncertainties (Abbott et al. 2020). In reality, stable remnants are expected to only represent a small fraction of GW170817-like events. Observations of future GW events are another route to quantifying $f_{\rm stable}$ (Margalit & Metzger 2019); although the largest challenge will be the precise localization of these events via EM counterparts, and the increasing sensitivity of future GW facilities that will result in dimmer counterparts for normal events.

A final avenue to constrain the fraction of stable remnants is via detection in untargeted radio surveys. Short GRBs are highly collimated, and the observed rate depends sensitively on their opening angles (Coward et al. 2012; Jin et al. 2018). Thus, the short GRB rate is likely a factor of $\approx$100 lower than the actual rate of BNS mergers (Fong et al. 2015). In contrast, the synchrotron radio signal from magnetar remnants is expected to be relatively isotropic, and thus every BNS merger that produces a stable remnant should in principle have an observable radio counterpart, regardless of the direction of the GRB jet. Therefore, radio remnants from stable magnetars should be bright radio signals and detectable in untargeted radio surveys, such as VLASS (Metzger et al. 2015b), and in turn offer an additional constraint on $f_{\rm stable}$.

Using the new light-curve modeling presented here, we calculate the instantaneous rate of radio signals from magnetar remnants found in a single VLASS epoch (Lacy et al. 2020), $N_{\rm VLASS}$, by adapting Equation (8) from Metzger et al. (2015b). Given the fractional sky coverage of VLASS ($f_{\rm VLASS} = 0.82$) and the typical rms of a single VLASS epoch ($F_{\nu,\rm VLASS} = 120\ \mu$Jy), this can be calculated as

$$N_{\rm VLASS} = f_{\rm VLASS} \times \frac{4\pi}{3}\left(\frac{L_\nu}{4\pi F_{\nu,\rm VLASS}}\right)^{3/2} \mathcal{R} t_{\rm dur}. \quad (4)$$

Here, L_ν is the spectral luminosity of the source in erg s^{-1} cm^{-2} Hz^{-1}, $\mathcal{R}$ is the volumetric rate of BNS mergers in Gpc^{-3} yr^{-1}, and $t_{\rm dur}$ is the survey timescale in years. To ensure a detection that is robust enough to detect variability, we fix L_ν to 1/10 of the peak luminosity for a given model (in effect requiring a 10σ detection). For the value of $\mathcal{R}$, we employ the local volumetric rate of BNS mergers derived from LIGO[12] ($\mathcal{R} = 250$–2810 Gpc^{-3} yr^{-1}; Abbott et al. 2020), and $t_{\rm dur} = 3$ yr (Metzger et al. 2015b).

To determine L_ν, we generate light-curve models for $E_{\rm ej} = 10^{53}$ erg (corresponding to stable remnants) at $\nu_{\rm VLASS} = 3$ GHz for varying densities, $n_0 = 10^{-3} - 1$ cm^{-3}. We show $N_{\rm VLASS}$ as a function of $f_{\rm stable}$ in Figure 7, and note that the peak luminosity for the 0.1 and 1 cm^{-3} cases are similar. For low circumburst densities of $n_0 \approx 10^{-3}$ cm^{-3}, only $\approx$0.1–1 are expected to be detected in VLASS in the most optimistic case where $f_{\rm stable} = 1$. On the other hand, if BNS mergers overall originate in higher-density environments (e.g., O'Connor et al. 2020; though see Fong et al. 2015), their radio remnants should be very luminous, and on the order of $\approx$30–300 should be detectable. Thus, comparing the VLASS-detected rate of radio remnants and the resulting constraint on $f_{\rm stable}$ with that from short GRBs will indirectly probe whether all BNS mergers produce short GRBs, and the connection between jet launching and remnant stability. In other words, if $\gtrsim$30–300 radio remnants are identified in VLASS, this is in tension with constraints from short GRBs and will indicate that the short GRB population is biased. Meanwhile, the non-detection of any radio remnants in VLASS will constrain the phase space of environment density and $f_{\rm stable}$, more so than is possible with cosmological short GRBs. Finally, we note the important caveat that $N_{\rm VLASS}$ only represents a detectable number in VLASS. The determination of whether or not a source is

[12] We note that this is not a 90% confidence interval, as the calculation involves the union of rates assuming a uniform mass distribution, and that derived from GW170817 and GW190425, but does properly represent the uncertainty in the latest rate estimates.

variable and can be properly identified as a remnant against the variable radio sky will necessarily be $< N_{\rm VLASS}$ (Metzger et al. 2015b).

7. Summary and Conclusions

We have presented new VLA radio limits of nine low-redshift short GRBs, which provide the most constraining power from the cosmological short GRB population on energy deposited by magnetars in kilonova ejecta. We have also presented a uniform reanalysis of all available radio limits at 5.5–6.0 GHz, alongside new light-curve modeling, which is an improvement on past models by properly incorporating relativistic effects and the deep-Newtonian regime. We come to the following conclusions:

1. With the low-redshift sample, we can place limits on the maximum ejecta energies of ≈ 0.6–6.7×10^{52} erg, assuming an ejecta mass of $0.03 M_\odot$. This increases to ≈ 1.8–17.6×10^{52} erg when considering larger ejecta masses of $0.1\ M_\odot$. For GW170817, we obtain a limit on the energy in the fastest kilonova ejecta of $E_{\rm ej,max} = 1.3 \times 10^{52}$ erg. Including all literature data, we find that the fraction of short GRBs that creates stable magnetars must not exceed ≈ 0.5–0.8.
2. We present predictions for the ejecta energies for varying $M_{\rm TOV}$, finding a bimodal distribution with peaks at $> 10^{52.5}$ erg, corresponding to indefinitely stable or a fraction of supramassive magnetar remnants, and peaks at $< 10^{50.5}$ erg, corresponding to the ejecta that are not boosted by magnetar energy deposition (i.e., cases where the remnant is a hypermassive NS or undergoes prompt collapse to a BH). Our short GRB limits consistently rule out indefinitely stable magnetars that deposit 10^{53} erg, and a fraction of supramassive NS cases.
3. Assuming the BNS merger mass distribution follows the Galactic distribution, the radio limits constrain $M_{\rm TOV} < 2.15\, M_\odot$, at 2σ confidence (statistical significance), slightly deeper than existing constraints. Motivated by the discovery of the high-mass BNS merger GW190425, an increasing fraction of high-mass mergers quickly weakens these constraints. We find a less stringent constraint of $M_{\rm TOV} < 2.23\, M_\odot$ (2σ) assuming a contribution of 40% high-mass mergers to the current population, and unconstraining limits on $M_{\rm TOV}$ when marginalized over this uncertain fraction. Our predictions can be compared to the true fraction of high-mass mergers as it is solidified with future GW detections.
4. We find that if current radio surveys such as VLASS were to detect tens to hundreds of stable magnetar remnants from BNS mergers, then this would imply that most short GRB remnants would be stable, which is at odds with current observations.

Going forward, a concerted effort to uncover radio remnants in surveys (e.g., VLASS, Lacy et al. 2020; ASKAP/VAST, Murphy et al. 2013; MeerKAT/ThunderKAT, Fender et al. 2016), in parallel with dedicated follow-up observations of local BNS mergers (detected via GWs or low-redshift short GRBs) will help to constrain the fraction of stable remnants. In particular, the rate of detection of luminous radio remnants compared to the constraints from short GRBs will indirectly address whether short GRBs are a biased population, and how the launching of a successful GRB jet is connected to remnant stability. Moreover, as GW facilities delineate the true mass distribution of BNS mergers with additional discoveries, these can be used in conjunction with short GRB limits to place stringent constraints on the value of $M_{\rm TOV}$ and the NS equation of state.

Support for G.S. in this work was provided by the NSF through Student Observing Support award SOSP19B-001 from the NRAO. The Fong Group at Northwestern acknowledges support by the National Science Foundation under grant Nos. AST-1814782 and AST-1909358. B.M. is supported by NASA through the NASA Hubble Fellowship grant #HST-HF2-51412.001-A awarded by the Space Telescope Science Institute, which is operated by the Association of Universities for Research in Astronomy, Inc., for NASA, under contract NAS5-26555. B.D.M. is supported in part by the Simons Foundation through the Simons Fellows Program (grant # 606260). K.D.A. is supported by NASA through the NASA Hubble Fellowship grant #HST-HF2-51403.001-A awarded by the Space Telescope Science Institute, which is operated by the Association of Universities for Research in Astronomy, Inc., for NASA, under contract NAS5-26555.

The National Radio Astronomy Observatory is a facility of the National Science Foundation operated under cooperative agreement by Associated Universities, Inc. This work made use of data supplied by the UK Swift Science Data Centre at the University of Leicester. This research was supported in part through the computational resources and staff contributions provided for the Quest high performance computing facility at Northwestern University, which is jointly supported by the Office of the Provost, the Office for Research, and Northwestern University Information Technology. The LBT is an international collaboration among institutions in the United States, Italy, and Germany. LBT Corporation partners are: The University of Arizona on behalf of the Arizona university system; Istituto Nazionale di Astrofisica, Italy; LBT Beteiligungsgesellschaft, Germany, representing the Max-Planck Society, the Astrophysical Institute Potsdam, and Heidelberg University; The Ohio State University, and The Research Corporation, on behalf of The University of Notre Dame, University of Minnesota, and University of Virginia.

Facilities: VLA, LBT:MODS.

Software: CASA (McMullin et al. 2007), aoflagger (Offringa et al. 2010, 2012), pwkit (Williams et al. 2017), RNS (Stergioulas & Friedman 1995).

ORCID iDs

Genevieve Schroeder https://orcid.org/0000-0001-9915-8147
Ben Margalit https://orcid.org/0000-0001-8405-2649
Wen-fai Fong https://orcid.org/0000-0002-7374-935X
Brian D. Metzger https://orcid.org/0000-0002-4670-7509
Peter K. G. Williams https://orcid.org/0000-0003-3734-3587
Kerry Paterson https://orcid.org/0000-0001-8340-3486
Kate D. Alexander https://orcid.org/0000-0002-8297-2473
Tanmoy Laskar https://orcid.org/0000-0003-1792-2338
Armaan V. Goyal https://orcid.org/0000-0001-9652-8384
Edo Berger https://orcid.org/0000-0002-9392-9681

References

Abbott, B. P., Abbott, R., Abbott, T. D., et al. 2017a, ApJL, 848, L13
Abbott, B. P., Abbott, R., Abbott, T. D., et al. 2017b, PhRvL, 119, 161101
Abbott, B. P., Abbott, R., Abbott, T. D., et al. 2020, ApJL, 892, L3
Ai, S., Gao, H., Dai, Z.-G., et al. 2018, ApJ, 860, 57

Antoniadis, J., Freire, P. C. C., Wex, N., et al. 2013, Sci, 340, 448
Arcavi, I. 2018, ApJL, 855, L23
Ascenzi, S., Coughlin, M. W., Dietrich, T., et al. 2019, MNRAS, 486, 672
Bauswein, A., Baumgarte, T. W., & Janka, H. T. 2013, PhRvL, 111, 131101
Belczynski, K., Klencki, J., Fields, C. E., et al. 2020, A&A, 636, A104
Beniamini, P., & van der Horst, A. J. 2017, MNRAS, 472, 3161
Bennett, C. L., Larson, D., Weiland, J. L., & Hinshaw, G. 2014, ApJ, 794, 135
Berger, E. 2014, ARA&A, 52, 43
Berger, E., Fong, W., & Chornock, R. 2013, ApJL, 774, L23
Bernuzzi, S. 2020, arXiv:2004.06419
Bloom, J. S., Perley, D. A., Chen, H.-W., et al. 2007, ApJ, 654, 878
Bloom, J. S., Prochaska, J. X., Pooley, D., et al. 2006, ApJ, 638, 354
Bucciantini, N., Metzger, B. D., Thompson, T. A., & Quataert, E. 2012, MNRAS, 419, 1537
Capano, C. D., Tews, I., Brown, S. M., et al. 2020, NatAs, 4, 625
Castro-Tirado, A. J., Sanchez-Ramirez, R., Lombardi, G., & Rivero, M. A. 2015, GCN, 17758, 1
Chornock, R., & Fong, W. 2015, GCN, 17358, 1
Condon, J. J., Cotton, W. D., Greisen, E. W., et al. 1998, AJ, 115, 1693
Coughlin, M. W., Dietrich, T., Doctor, Z., et al. 2018, MNRAS, 480, 3871
Coughlin, M. W., Dietrich, T., Margalit, B., & Metzger, B. D. 2019, MNRAS, 489, L91
Coward, D. M., Howell, E. J., Piran, T., et al. 2012, MNRAS, 425, 2668
Cromartie, H. T., Fonseca, E., Ransom, S. M., et al. 2020, NatAs, 4, 72
Cucchiara, A., Prochaska, J. X., Perley, D., et al. 2013, ApJ, 777, 94
Demorest, P. B., Pennucci, T., Ransom, S. M., Roberts, M. S. E., & Hessels, J. W. T. 2010, Natur, 467, 1081
de Ugarte Postigo, A., Thöne, C. C., Rowlinson, A., et al. 2014, A&A, 563, A62
Eldridge, J. J., Stanway, E. R., & Tang, P. N. 2019, MNRAS, 482, 870
Evans, P. A., Beardmore, A. P., Page, K. L., et al. 2009, MNRAS, 397, 1177
Fan, Y.-Z., Wu, X.-F., & Wei, D.-M. 2013, PhRvD, 88, 067304
Fender, R., Woudt, P. A., Corbel, S., et al. 2016, in MeerKAT Science On the Pathway to the SKA, 13 (Trieste: SISSA)
Fong, W. 2015, GCN, 17804, 1
Fong, W., Alexander, K. D., & Laskar, T. 2016a, GCN, 19854, 1
Fong, W., Berger, E., Blanchard, P. K., et al. 2017, ApJL, 848, L23
Fong, W., Berger, E., Margutti, R., & Zauderer, B. A. 2015, ApJ, 815, 102
Fong, W., Berger, E., Metzger, B. D., et al. 2014, ApJ, 780, 118
Fong, W., Metzger, B. D., Berger, E., & Özel, F. 2016b, ApJ, 831, 141
Foucart, F. 2012, PhRvD, 86, 124007
Gao, H., Zhang, B., & Lü, H.-J. 2016, PhRvD, 93, 044065
Gehrels, N., Chincarini, G., Giommi, P., et al. 2004, ApJ, 611, 1005
Gehrels, N., Sarazin, C. L., O'Brien, P. T., et al. 2005, Natur, 437, 851
Giacomazzo, B., & Perna, R. 2013, ApJL, 771, L26
Gompertz, B. P., Levan, A. J., & Tanvir, N. R. 2020, ApJ, 895, 58
Gompertz, B. P., O'Brien, P. T., Wynn, G. A., & Rowlinson, A. 2013, MNRAS, 431, 1745
Granot, J., Piran, T., & Sari, R. 1999, ApJ, 527, 236
Granot, J., & Sari, R. 2002, ApJ, 568, 820
Hajela, A., Margutti, R., Alexander, K. D., et al. 2019, ApJL, 886, L17
Horesh, A., Hotokezaka, K., Piran, T., Nakar, E., & Hancock, P. 2016, ApJL, 819, L22
Hotokezaka, K., & Piran, T. 2015, MNRAS, 450, 1430
Huang, Y. F., Dai, Z. G., & Lu, T. 1999, MNRAS, 309, 513
Intema, H. T., van der Tol, S., Cotton, W. D., et al. 2009, A&A, 501, 1185
Jin, Z.-P., Li, X., Wang, H., et al. 2018, ApJ, 857, 128
Kasen, D., Fernández, R., & Metzger, B. D. 2015, MNRAS, 450, 1777
Kiuchi, K., Kyutoku, K., Sekiguchi, Y., Shibata, M., & Wada, T. 2014, PhRvD, 90, 041502
Kiziltan, B., Kottas, A., De Yoreo, M., & Thorsett, S. E. 2013, ApJ, 778, 66
Klose, S., Nicuesa Guelbenzu, A. M., Michałowski, M. J., et al. 2019, ApJ, 887, 206
Knust, F., Greiner, J., van Eerten, H. J., et al. 2017, A&A, 607, A84
Lacy, M., Baum, S. A., Chandler, C. J., et al. 2020, PASP, 132, 035001
Lamb, G. P., Tanvir, N. R., Levan, A. J., et al. 2019, ApJ, 883, 48
Lasky, P. D., Haskell, B., Ravi, V., Howell, E. J., & Coward, D. M. 2014, PhRvD, 89, 047302
Lattimer, J. M., & Prakash, M. 2016, PhR, 621, 127
Lawrence, S., Tervala, J. G., Bedaque, P. F., & Miller, M. C. 2015, ApJ, 808, 186
Lien, A., Sakamoto, T., Barthelmy, S. D., et al. 2016, ApJ, 829, 7
LIGO Scientific Collaboration & Virgo Collaboration 2019, PhRvX, 9, 031040
Liu, L.-D., Gao, H., & Zhang, B. 2020, ApJ, 890, 102
Lü, H.-J., Zhang, B., Lei, W.-H., Li, Y., & Lasky, P. D. 2015, ApJ, 805, 89
Makhathini, S., Mooley, K. P., Brightman, M., et al. 2020, arXiv:2006.02382
Margalit, B., & Metzger, B. D. 2017, ApJL, 850, L19
Margalit, B., & Metzger, B. D. 2019, ApJL, 880, L15
Margalit, B., Metzger, B. D., & Beloborodov, A. M. 2015, PhRvL, 115, 171101
Margalit, B., & Piran, T. 2015, MNRAS, 452, 3419
Margalit, B., & Piran, T. 2020, MNRAS, 495, 4981
Margutti, R., Alexander, K. D., Xie, X., et al. 2018, ApJL, 856, L18
Marshall, F. E., & Beardmore, A. P. 2015, GCN, 17751, 1
McMullin, J. P., Waters, B., Schiebel, D., Young, W., & Golap, K. 2007, in ASP Conf. Ser. 376, Astronomical Data Analysis Software and Systems XVI, ed. R. A. Shaw, F. Hill, & D. J. Bell (San Francisco, CA: ASP), 127
Metzger, B. D., & Bower, G. C. 2014, MNRAS, 437, 1821
Metzger, B. D., & Fernández, R. 2014, MNRAS, 441, 3444
Metzger, B. D., Margalit, B., Kasen, D., & Quataert, E. 2015a, MNRAS, 454, 3311
Metzger, B. D., & Piro, A. L. 2014, MNRAS, 439, 3916
Metzger, B. D., Quataert, E., & Thompson, T. A. 2008, MNRAS, 385, 1455
Metzger, B. D., Thompson, T. A., & Quataert, E. 2018, ApJ, 856, 101
Metzger, B. D., Williams, P. K. G., & Berger, E. 2015b, ApJ, 806, 224
Mösta, P., Radice, D., Haas, R., Schnetter, E., & Bernuzzi, S. 2020, arXiv:2003.06043
Murase, K., Toomey, M. W., Fang, K., et al. 2018, ApJ, 854, 60
Murguia-Berthier, A., Ramirez-Ruiz, E., Montes, G., et al. 2017, ApJL, 835, L34
Murphy, T., Chatterjee, S., Kaplan, D. L., et al. 2013, PASA, 30, e006
Nakar, E., & Piran, T. 2011, Natur, 478, 82
Nava, L., Sironi, L., Ghisellini, G., Celotti, A., & Ghirlanda, G. 2013, MNRAS, 433, 2107
Noordam, J. E. 2004, Proc. SPIE, 5489, 817
Norris, J. P., Barthelmy, S. D., Cummings, J. R., & Gehrels, N. 2015, GCN, 17759, 1
O'Connor, B., Beniamini, P., & Kouveliotou, C. 2020, MNRAS, 495, 4782
Offringa, A. R., de Bruyn, A. G., Biehl, M., et al. 2010, MNRAS, 405, 155
Offringa, A. R., van de Gronde, J. J., & Roerdink, J. B. T. M. 2012, A&A, 539, A95
Panaitescu, A., & Kumar, P. 2001, ApJL, 560, L49
Pe'er, A. 2012, ApJL, 752, L8
Perley, D. A., Modjaz, M., Morgan, A. N., et al. 2012, ApJ, 758, 122
Perley, D. A., & Perley, R. A. 2013, ApJ, 778, 172
Piran, T., Nakar, E., & Rosswog, S. 2013, MNRAS, 430, 2121
Piro, A. L., Giacomazzo, B., & Perna, R. 2017, ApJL, 844, L19
Pooley, D., Kumar, P., Wheeler, J. C., & Grossan, B. 2018, ApJL, 859, L23
Radice, D., Perego, A., Hotokezaka, K., et al. 2018, ApJ, 869, 130
Rowlinson, A., O'Brien, P. T., Metzger, B. D., Tanvir, N. R., & Levan, A. J. 2013, MNRAS, 430, 1061
Ruiz, M., & Shapiro, S. L. 2017, PhRvD, 96, 084063
Ryan, G., van Eerten, H., MacFadyen, A., & Zhang, B.-B. 2015, ApJ, 799, 3
Sari, R., Piran, T., & Narayan, R. 1998, ApJL, 497, L17
Sarin, N., Lasky, P. D., & Ashton, G. 2020, PhRvD, 101, 063021
Sault, R. J., & Wieringa, M. H. 1994, A&AS, 108, 585
Shibata, M., Fujibayashi, S., Hotokezaka, K., et al. 2017, PhRvD, 96, 123012
Shibata, M., & Taniguchi, K. 2006, PhRvD, 73, 064027
Shibata, M., Zhou, E., Kiuchi, K., & Fujibayashi, S. 2019, PhRvD, 100, 023015
Siegel, D. M., & Metzger, B. D. 2017, PhRvL, 119, 231102
Sironi, L., & Giannios, D. 2013, ApJ, 778, 107
Spitkovsky, A. 2008, ApJL, 682, L5
Stergioulas, N., & Friedman, J. L. 1995, ApJ, 444, 306
Stratta, G., Dainotti, M. G., Dall'Osso, S., Hernandez, X., & De Cesare, G. 2018, ApJ, 869, 155
Tanvir, N. R., Levan, A. J., Fruchter, A. S., et al. 2013, Natur, 500, 547
Troja, E., Sakamoto, T., Cenko, S. B., et al. 2016, ApJ, 827, 102
van der Horst, A. J., Wiersema, K., & Wijers, R. A. M. J. 2005, GCN, 3405, 1
Villar, V. A., Guillochon, J., Berger, E., et al. 2017, ApJL, 851, L21
Wiersema, K., Levan, A., Cenko, S. B., & Tanvir, N. 2013, GCN, 15178, 1
Williams, P. K. G., Allers, K. N., Biller, B. A., & Vos, J. 2019, RNAAS, 3, 110
Williams, P. K. G., Clavel, M., Newton, E., & Ryzhkov, D. 2017, pwkit: Astronomical Utilities in Python, Astrophysics Source Code Library, ascl:1704.001
Yu, Y.-W., Zhang, B., & Gao, H. 2013, ApJL, 776, L40
Yun, M. S., & Carilli, C. L. 2002, ApJ, 568, 88
Zhang, B., & Mészáros, P. 2001, ApJL, 552, L35